Bifurcation analysis of ocean, atmosphere and climate models

Eric Simonnet, Henk A. Dijkstra, Michael Ghil

Institut Non Linéaire de Nice, UMR6612, CNRS, France.
Institute for Marine and Atmospheric research Utrecht, Utrecht, The Netherlands.
Département Terre-Atmosphère-Océan, Ecole Normale Supérieure,
and Laboratoire de Météorologie Dynamique (CNRS and IPSL), Paris, France,
and Atmospheric and Oceanic Sciences Department
and Institute of Geophysics and Planetary Physics,
University of California, Los Angeles, USA

Abstract

We provide an overview of numerical bifurcation methods and how they can help one understand the variability of large-scale oceanic and atmospheric flows, as well of the climate system as a whole. As a particular example, we consider the problem of how low-frequency variability of the wind-driven ocean circulation arises due to internal dynamics. The methods are illustrated with the help of a hierarchy of models of so-called double-gyre, wind-driven flows.

1 Introduction

The climate system is highly complex. It is composed of many subsystems, each with its own characteristic time scales, spatial scales, and physical complexities. To better describe, understand and predict how the climate is evolving requires an in-depth understanding of these subsystems and how they interact with each other. Up until today, even the most sophisticated, high-resolution, global earth-system models are unable to provide accurate and reliable simulations of climate change, subject to both natural and anthropogenic forcing. Although it is now possible to predict some general tendencies of atmospheric and oceanic fields over several decades, many quantitative as well as qualitative aspects of climate change are still far from being well understood. The main difficulties are related not only to the turbulent behavior of the smaller scales of motion, and their effects on the large scales, but also to a lack of understanding of the physics driving the whole system.

A key prerequisite to greater scientific insight into the climate system as a whole is the availability of a hierarchy of climate models, from the highly simplified to the

very detailed. Relying on such a model hierarchy is probably the most reasonable strategy for understanding fundamental aspects of climate change [1, 2, 3, 4]. This strategy aims at increasing our knowledge of the system from its most basic to its highly applied aspects; it does so by studying, on the one hand, each subsystem in isolation, from the bottom up, while on the other it considers increasingly complex versions of the whole system in combination.

The case of the oceans is particularly illuminating. The simplest zero-dimensional ocean models are represented by a small number of ordinary differential equations (ODEs), typically O(10) at most, which are referred to as box models. They are, for example, used to study the stability of the oceans' thermohaline circulation [5]. One-dimensional partial differential equation (PDE) models can also be used to study the vertical structure of the upper ocean alone or the oceanic mixed layer.

Two-dimensional PDE models of the oceans correspond to models that resolve either the two horizontal coordinates (x, y), like in traditional studies of the wind-driven ocean circulation [6, 7] (see also section 4.1, [8, 3]) or a vertical vs. an horizontal coordinate (y, z), like in studies of the thermohaline circulation [9, 10, 11, 12]. Finally, general circulation models (GCMs) or primitive-equation models (PEs) are essentially 3-D models that are composed of several subsystems coupled with each other. These models, such as coupled ocean-atmosphere models, include both dynamical and thermodynamical processes. Results from GCMs are, in general, difficult to interpret without the knowledge accumulated from the study of lower- dimensional models, but are essential for understanding climate change.

The hierarchy of models outlined above must not hide the fact that complexity increases not only in the dimensionality of the models but in several directions at once. This is especially true when one considers PDE models. Apart from the physical processes, which are already included, one may consider two other directions of increasing complexity. First, as one increases the spatial resolution of a PDE model, the effects of the unresolved, turbulent small scales on the resolved, large scales become crucial; sophisticated techniques to parametrise these subgrid-scale effects are part of the success of any GCM. Indeed, as one increases the spatial resolution, new phenomena may appear which were completely ignored or neglected before. A recent and striking example can be given regarding the influence of oceanic fronts on the atmosphere above, where new instabilities emerge in eddy-resolving 2-D models [13, 14]. These instabilities are not found in coarse-resolution GCMs (see also [15]). Second, the geometry of the problem — e.g., the shape of the domain and the spatial structure of the forcing — is also an important factor that cannot be neglected and plays a key role in bringing the model problem closer to reality. Figure 1 illustrates the three axes of increasing complexity described herein.

In confronting modeling results with observations one has to realize that it is the largest scales that are best and most reliably captured. The variability of the large scales arises from two sources: (i) the competition among the finite-amplitude

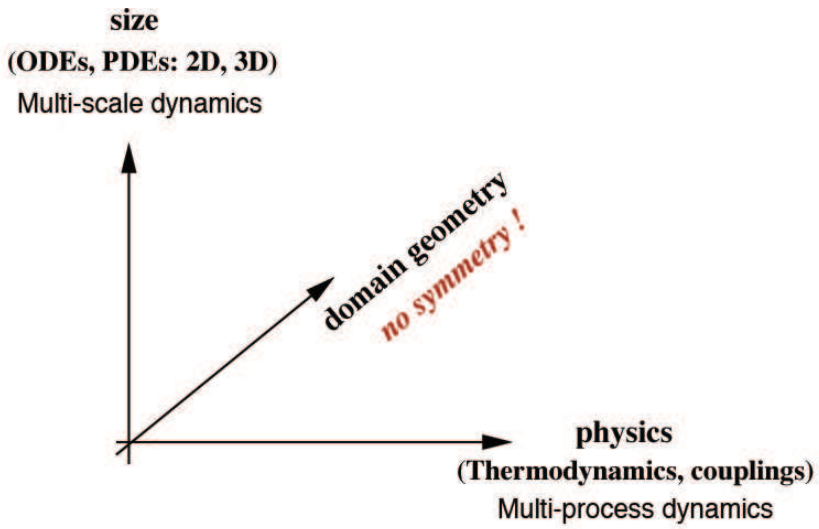

Figure 1: Directions of increasing complexity in a hierarchy of models.

instabilities; and (ii) the net effects of the smaller scales. In many situations, in the atmosphere as well as in the ocean, the analysis of climate data shows that the large-scale flows exhibit quasi-periodic behavior, with strongly localized spectral peaks emerging above the background red-noise spectrum. This feature might indicate that the weakly turbulent large scales are dominated by low-dimensional dynamics; in other words, at specific scales, some form of approximate closure might exist. A typical example is given by the low-frequency dynamics of the wind-driven ocean circulation, where certain large-scale instabilities are almost unaffected by the small-scale eddies, due to a significant spectral gap between these scales. These instabilities are related to the existence of homoclinic cycles and strange attractors of very low dimension [16, 17]. A more detailed description is given in section 4.

Dynamical systems theory thus appears to provide a good set of tools to study the large-scale dynamics and in particular to address the first source of variability above. This theory is particularly efficient at explaining how chaotic behavior of small-dimensional systems emerges and the phase transitions and bifurcations that might lead from simple to more complex behavior. The theory is most fully developed for systems with a finite number of degrees of freedom. However, the remarks above might give the reader some hint of why it appears very promising in the context of climate studies. We will also comment in the last section on the second source of variability, that is, the effects of the small scales on the large ones.

Most of the PDE systems that govern climate dynamics are dissipative and possess finite-dimensional attractors, as well as nice regularity properties. A specific solution of such a system — for given initial and boundary data and a fixed set of parameter values — may be considered as a single point in a suitably defined function space.

Such a solution evolves along a deterministic trajectory and belongs to an associated semi-group of solutions for different initial data. In general, these solutions asymptotically converge to a global attractor of finite but still fairly large dimension [18]. An important aspect of climate studies is to probe these attractors so as to extract their topological and metric properties. This approach can provide some predictive answers to the following questions:

1. what are the generic transition routes to chaos in these systems?
2. how well do these routes explain the climate system's observed behavior?
3. how sensitive is this behavior to natural or anthropogenic perturbations?

We cannot present, in the allotted space, a global method to answer all these questions but will concentrate instead on some numerical techniques to succeed in a less ambitious although highly pertinent quest: how to extract local properties of the PDEs attractors? This presentation will mostly focus on bifurcation theory and its numerical applications.

Our aim is to describe numerical algorithms for computing in a rather simple way the branches of steady states and periodic orbits of geophysical flows that are governed by systems of nonlinear PDES. A by-product of these algorithms is to help detect the bifurcations of these steady and periodic solutions. Bifurcation theory is outlined in section 2. Its applications to the numerical computation of branches of steady states and periodic orbits are given in section 3. In section 4, we describe a typical example of the application of these techniques to a hierarchy of models of the wind-driven ocean circulation. An outlook on future developments is provided in section 5.

2 Bifurcation theory

Bifurcation theory studies changes in the qualitative behavior of a dynamical system as one or several of its parameters vary. The results of this theory permit one to follow systematically climatic behavior from the simplest kind of model solutions to the most complex, from single to multiple equilibria, periodic, chaotic to fully turbulent solutions. Through our approach, we mainly aim to detect local bifurcations, that is, in situations where the only knowledge of the leading eigenvalues of the linearized equations is enough to conclude on the phase-space dynamics. We will also give some examples of global bifurcations such as homoclinic ones that are surprisingly common in climate models [19, 20, 21, 22].

Here we sketch the basics concepts of bifurcation theory for a general system of autonomous ODEs of dimension n that can be written as

$$\frac{d\mathbf{x}}{dt} = \mathbf{f}(\mathbf{x}, \mathbf{p}). \tag{1}$$

Here $\mathbf{x}$ is the state vector in the phase space $\mathbb{R}^n$ which typically corresponds to the discretized solutions of the PDE models using either finite differences, finite elements or spectral methods. Although we do not assume here that the number of degrees of freedom n is large, it must be kept in mind that it is of the order of $O(10^4)$ for 2-D PDEs and $O(10^{5-6})$ for 3-D models. The vector $\mathbf{p}$ is the parameter vector in $\mathbb{R}^p$ where p is usually much smaller than n and for now on we choose $p = 1$, that is we consider bifurcations that appear through variation of one parameter only; these bifurcations are usually referred to as codimension-1 bifurcations. The right-hand side $\mathbf{f}$ contains the model dynamics including the forcing terms and it depends on $\mathbf{x}$ in a nonlinear fashion, at time t. We also restrict here the discussion to autonomous systems, that is, $\mathbf{f}$ does not depend explicitly on time. A trajectory of the dynamical system, starting at the initial state $\mathbf{x}(t_0) = \mathbf{x}_0$, is a curve $\Gamma = \{\mathbf{x}(t); -\infty < t < \infty\}$ in $\mathbb{R}^n$ which satisfies (1). The solution at time t with initial condition $\mathbf{x}_0$ will be indicated later on $\phi_t(\mathbf{x}_0)$. In the following we will refer to the solution $\bar{\mathbf{x}}$ of

$$\mathbf{f}(\bar{\mathbf{x}}, \bar{\mathbf{p}}) = 0, \tag{2}$$

as a fixed point or equilibrium for which $\mathbf{x}(t) = \bar{\mathbf{x}}$ for all t, or also a steady state in the context of PDEs.

Linear stability analysis of a particular fixed point $(\bar{\mathbf{x}}, \bar{\mathbf{p}})$ amounts to consider infinitesimally small perturbations $\mathbf{y}$, i.e.

$$\mathbf{x} = \bar{\mathbf{x}} + \mathbf{y}; \tag{3}$$

linearization of (1) around $\bar{\mathbf{x}}$ then gives

$$\frac{d\mathbf{y}}{dt} = \mathbf{J}(\bar{\mathbf{x}}, \bar{\mathbf{p}})\mathbf{y}, \tag{4}$$

where $\mathbf{J}$ is the Jacobian matrix

$$\mathbf{J} = \begin{pmatrix} \frac{\partial f_1}{\partial x_1} & \cdots & \frac{\partial f_1}{\partial x_n} \\ \cdots & \cdots & \cdots \\ \frac{\partial f_n}{\partial x_1} & \cdots & \frac{\partial f_n}{\partial x_n} \end{pmatrix}. \tag{5}$$

The linear autonomous ODE system (4) has solutions of the form $\mathbf{y}(t) = \mathrm{e}^{\sigma t}\hat{\mathbf{y}}$. Substituting such a solution into (4) leads to an eigenvalue problem for the complex growth factor $\sigma = \sigma_r + i\sigma_c$ where $i^2 = -1$, namely

$$\mathbf{J}(\bar{\mathbf{x}}, \bar{\mathbf{p}})\hat{\mathbf{y}} = \sigma\hat{\mathbf{y}}. \tag{6}$$

Fixed points for which there are eigenvalues with $\sigma_r > 0$ are unstable since the associated perturbations are exponentially growing, whereas fixed points for which

$\sigma_r < 0$ are linearly stable. In the situation where $\sigma_c \neq 0$ the associated eigenmodes will be oscillatory with frequency σ_c, i.e. with a characteristic period of $2\pi/\sigma_c$. The eigenspaces associated with eigenvalues $\sigma_r > 0$ (resp. $\sigma_r < 0$) will be denoted E^u (resp. E^s) whereas the eigenspace associated with eigenvalues $\sigma_r = 0$ will be denoted E^c.

Before enumerating the various possible codimension-1 bifurcations, we briefly recall some basics and essential notions of dynamical systems theory.

Theorem 1 (Hartman-Grobman)*: if* $\mathbf{J}(\bar{\mathbf{x}}, \bar{\mathbf{p}})$ *has no purely imaginary eigenvalues, the number of eigenvalues with positive and negative real parts determine the topological equivalence (homeomorphism) of the flow near* $\bar{\mathbf{x}}$*.*

This result roughly says that the local structure of the flow near the fixed point is structurally stable. In such a case, $\bar{\mathbf{x}}$ is called an *hyperbolic* fixed point. Bifurcations correspond precisely to situations where this theorem does not apply, that is, where the flow is not structurally stable. The *stable* (W^s) and *unstable* (W^u) *manifolds* are defined as

$$\begin{aligned} W^s(\bar{\mathbf{x}}) &= \{\mathbf{x} \mid \lim_{t\to+\infty} \phi_t(\mathbf{x}) = \bar{\mathbf{x}}\} \\ W^u(\bar{\mathbf{x}}) &= \{\mathbf{x} \mid \lim_{t\to-\infty} \phi_t(\mathbf{x}) = \bar{\mathbf{x}}\} \end{aligned} . \tag{7}$$

These manifolds are unique and are tangent to the corresponding eigenspaces E^u and E^s of the linearized system (6) at $\bar{\mathbf{x}}$. The situation where bifurcations occur, that is, there are n_0 eigenvalues with vanishing real part, $\sigma_r = 0$, lead to the center manifold theorem:

Theorem 2 *There exist unique stable and unstable manifolds* W^u *and* W^s *tangent to* E^u *and* E^s *at* $\bar{\mathbf{x}}$ *and a (nonunique) center manifold* W^c *tangent to* E^c *at* $\bar{\mathbf{x}}$*. The three manifolds are all invariant by the flow* ϕ_t*.*

The center manifold is in general associated with a loss of regularity contrary to the unstable and stable manifolds. Theorem 2 indeed implies that it is possible to reduce (locally) the dynamics on the center manifold, typically, taking $\bar{\mathbf{x}} = 0$ for simplicity, one has

$$\frac{d\mathbf{u}}{dt} = \mathbf{L}_0\mathbf{u} + \mathbf{N}(\mathbf{u}, \mathbf{p}), \tag{8}$$

where $\mathbf{N}$, which depends on the vector parameter $\mathbf{p}$, has a Taylor expansion starting with at least quadratic terms, $\mathbf{u}$ lives in $\mathbf{R}^{n_0}$ and $\mathbf{L}_0$ has n_0 eigenvalues with zero real part. Another well-known approach is the Lyapunov-Schmidt reduction that we do not present here [23, 24].

Having reduced the system (1) into the system (8) it is possible to find a change of coordinates (e.g. $\mathbf{u} = \mathbf{v} + H(\mathbf{v})$ for the system (8)) so that the system becomes 'as simple as possible'. The resulting vector field thus obtained is called the *normal form*. It is an extension of the reduction to Jordan form for matrices to the nonlinear case.

Normal form theory provides a way to classify the different kind of bifurcations that may occur with only knowledge of the eigenvalues that lie on the imaginary axis. We do not present normal form theory in this short presentation, the reader may refer to [25, 26] for further details.

2.1 Local codimension-1 bifurcations of steady states

We are now ready to present the most important bifurcation cases, starting with the situation of a single zero eigenvalue ($n_0 = 1$). In this case, there are three important normal forms:

1. Saddle-node bifurcation: it corresponds to the case where the system (8) (when reduced to its normal form) is

$$\dot{u} = p \pm u^2. \tag{9}$$

The sign characterizes supercriticality ($p - u^2$) or subcriticality ($p + u^2$). In the supercritical case, it is straightforward to check that the branch of solutions $u = \sqrt{p}$ is stable and the branch $u = -\sqrt{p}$ is unstable (see Fig. 2).

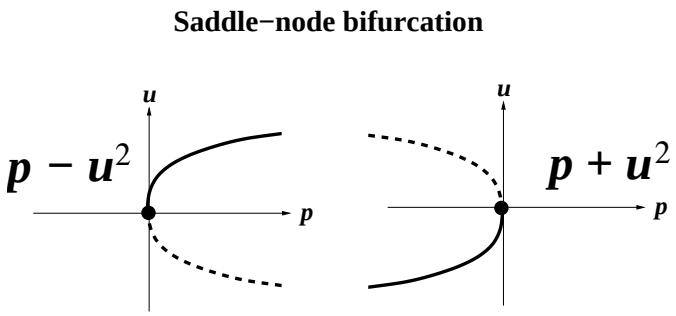

Figure 2: Supercritical (left) and subcritical (right) saddle-node bifurcation. The solid (dotted) branches indicate stable (unstable) solutions.

2. Transcritical bifurcation: the normal form corresponds in this case to

$$\dot{u} = pu \pm u^2. \tag{10}$$

3. Pitchfork bifurcation (symmetry breaking): the normal form is

$$\dot{u} = pu \pm u^3. \tag{11}$$

In the supercritical situation, there is a transfer of stability from the symmetric solution $u = 0$ to the pair of conjugated solutions $u = \pm\sqrt{p}$ (see Fig. 4). In the

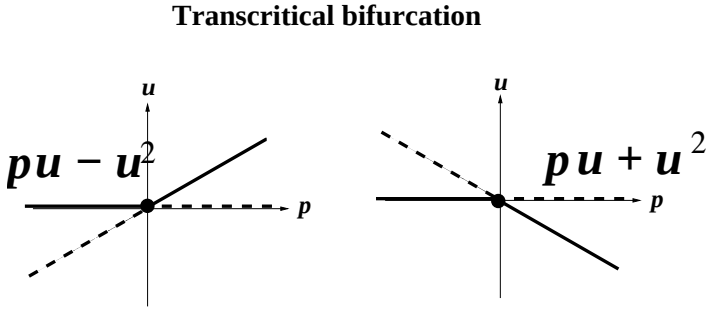

Figure 3: Supercritical (left) and subcritical (right) transcritical bifurcation.

supercritical case, it must be noted that the system remains in a neighborhood of the equilibrium so that one observes a *soft* or *noncatastrophic* loss of stability. In the subcritical case, the situation is very different as can been seen in the left panel of Fig. 4. the domain of attraction of the fixed point is bounded by the unstable ones and shrinks as the parameter p approaches zero to disappear. The system is thus pushed out from the neighborhood of the now unstable fixed point leading to a *sharp* or *catastrophic* loss of stability. Decreasing again the parameter to negative values will not return the system to the previously stable equibrium since it may have already left its domain of attraction.

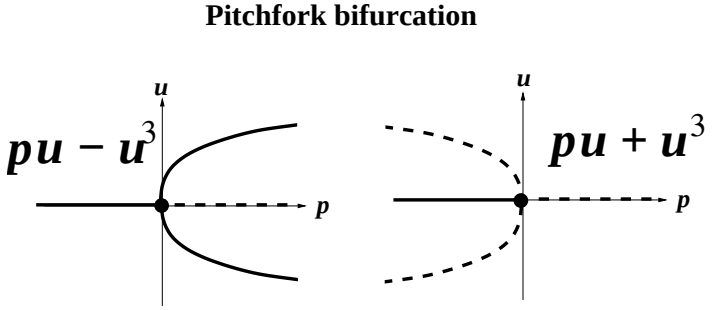

Figure 4: Supercritical (left) and subcritical (right) pitchfork bifurcation.

The importance of the saddle-node case is that all codimension-1 bifurcations with a zero eigenvalue can be perturbed to saddle-node bifurcations (see Fig. 5). These perturbations arise through imperfections of the physical system, domain geometry, boundary conditions, or forcing terms. The last two cases (pitchfork and transcritical) indeed illustrate situations where there is something special about the formulation of the problem: the pitchfork bifurcation is the rule for systems constrained by some (e.g., reflection) symmetry.

Whereas in the previous cases, the number of fixed points changed as the parameter was varied, it is also possible that a steady solution transfers its stability to a limit

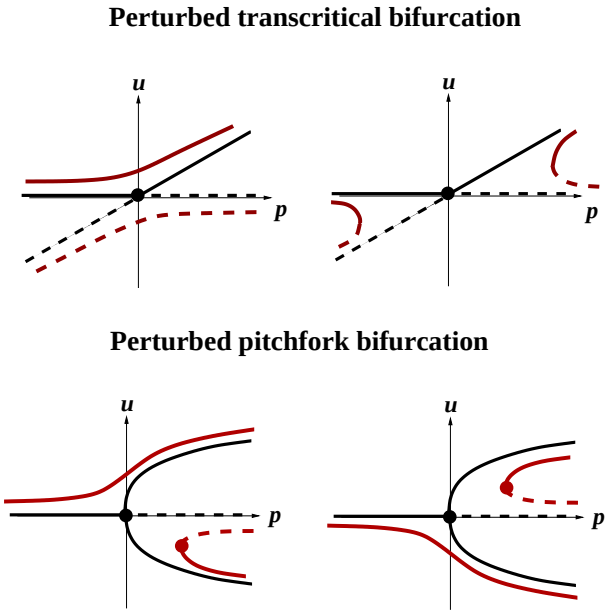

Figure 5: Perturbed transcritical bifurcation (upper panel) and perturbed pitchfork bifurcation (lower panel). The left and right panels for each case are different possibilities arising from a perturbation of each normal form.

cycle. This kind of transition is called a Hopf bifurcation. It corresponds to the special case of a simple conjugate pair of pure imaginary eigenvalues $\sigma = \pm\omega i$ ($n_0 = 2$) crossing the imaginary axis. The normal form can be written in polar coordinate as

$$\begin{aligned} \dot{r} &= pr \pm r^3 \\ \dot{\theta} &= \omega \end{aligned} \quad . \tag{12}$$

Again the sign determines whether the Hopf bifurcation is supercritical or subcritical and the discussion is similar to the pitchfork bifurcation case. For more complete details on Hopf bifurcations see e.g. [27].

2.2 Local codimension-1 bifurcations of limit cycles

One may ask whether it is possible to apply the procedures described above to more complex (limit) sets. A very similar discussion applies for bifurcation of limit cycles although there are some additional complications. Let's assume that one has a limit cycle γ of the original system (1) for a parameter $\bar{p}$ that we omit in the notations for simplicity, and whose corresponding solution is $\bar{\mathbf{x}}(t) = \bar{\mathbf{x}}(t+T)$. We consider an infinitesimal perturbation $\xi(t)$ of γ, i.e., we let $\mathbf{x}(t) = \bar{\mathbf{x}}(t) + \xi(t)$ in (1) and neglecting quadratic terms, one obtains

$$\dot{\xi} = \mathbf{J}(\bar{\mathbf{x}}(t))\xi, \tag{13}$$

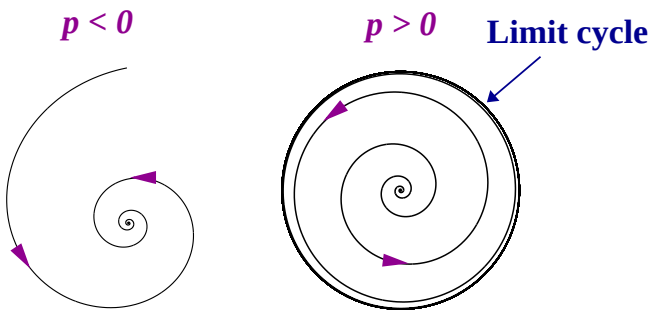

Figure 6: Phase space trajectories associated with a supercritical Hopf bifurcation at $p = 0$. For $p < 0$, there is only one stable fixed point (left panel), whereas a stable limit cycle appears for $p > 0$ (right panel).

and $\mathbf{J}(\bar{\mathbf{x}}(t))$ is now a T-periodic matrix. It can be shown that the fundamental solution matrix X of the system (13) can be written as $X(t) = Y(t)\mathrm{e}^{t\mathcal{R}}$ where $Y(t+T) = Y(t)$. One thus obtains that

$$X(t+T) = \mathbf{M}X(t),\ \mathbf{M} = \mathrm{e}^{T\mathcal{R}}. \tag{14}$$

The matrix $\mathbf{M}$ is called the *monodromy* matrix and its eigenvalues $\sigma_1, \cdots, \sigma_n$ are called the *Floquet multipliers*. The monodromy matrix is not uniquely determined by the solutions of (13) but its eigenvalues are uniquely determined. Since the perturbation $\xi(t) = \bar{\mathbf{x}}(t+\epsilon) - \bar{\mathbf{x}}(t)$, ϵ small, is T-periodic, it immediately implies that $\mathbf{M}$ has an unit eigenvalue, i.e. perturbations along γ neither diverge or converge. The linear stability of γ is thus determined by the remaining $n-1$ eigenvalues.

Let Σ be a (fixed) local cross section of dimension $n-1$ of the limit cycle γ such that the periodic orbit is not tangent to this hypersurface and denote $\mathbf{x}^\star$ the intersection of Σ with γ. There is a nice geometrical interpretation of the monodromy matrix in term of the Poincaré map defined as $\mathcal{P}(\mathbf{x}) = \phi_\tau(\mathbf{x})$, where $\mathbf{x}$ is assumed to be in a neighborhood of $\mathbf{x}^\star$ and, τ is the time taken for the orbit $\phi_t(\mathbf{x})$ to first return to Σ (as $\mathbf{x}$ approaches $\mathbf{x}^\star$ τ will tend to T). After a change of basis such that the matrix $\mathbf{M}$ has a column $(0, \cdots 0, 1)^T$ corresponding to the unit eigenvalue, the remaining block $(n-1) \times (n-1)$ matrix corresponds to the linearized Poincaré map.

These remarks show that the bifurcations of limit cycles are related to the behavior of a discrete dynamical system (the Poincaré map)

$$x_{n+1} = \mathcal{P}x_n, \tag{15}$$

rather than a continuous dynamical system like in the case of fixed points. The bifurcation theory for fixed points of the iterative map with eigenvalue having unit norm is completely analogous to the bifurcation theory for equilibria with an eigenvalue on the imaginary axis. Periodic orbits become unstable when Floquet multipliers

σ_i cross the unit circle as the parameter p is changed (remember that the Floquet multipliers depend on the parameter p). There are three important cases.

1. A real Floquet multiplier is crossing the unit circle $\sigma(\bar{p}) = 1$ (saddle-node). This situation can be shown to be topologically equivalent to the 1-dimensional discrete dynamical system

$$x_{n+1} = \mathcal{P}(x_n), \text{ with } \mathcal{P}(x) = p + x \pm x^2. \tag{16}$$

Let's consider the supercritical case $\mathcal{P}(x) = p + x - x^2$ and assume that $\bar{p} = 0$ for simplicity. As p becomes positive, two fixed points $x_1^\star$ and $x_2^\star$ of the iterative map (16) appear which are solutions of $\mathcal{P}(x) = x$. These two fixed points correspond to the appearance of 2 new families of periodic orbits. One family is stable ($\mathcal{P}'(x_1^\star) < 1$) while the other is unstable ($\mathcal{P}'(x_2^\star) > 1$). Like in the case of equilibria, particular constraints may lead to *transcritical* or *pitchfork* bifurcations (see Fig. 7).

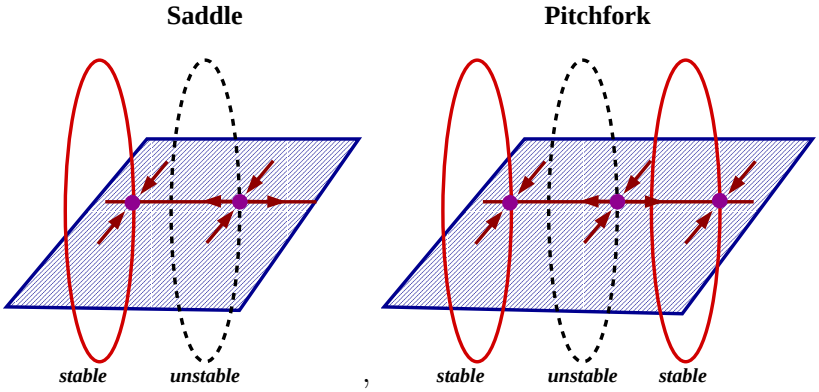

Figure 7: Phase space view associated with the saddle-node (left panel) and pitchfork (right panel) bifurcations of periodic orbits.

2. A real Floquet multiplier is crossing the unit circle with $\sigma(\bar{p}) = -1$. This situation is called *flip* or *period-doubling* bifurcation and has no equivalent for equilibria. The system is topologically equivalent to

$$x_{n+1} = \mathcal{P}(x_n), \text{ with } \mathcal{P}(x) = -(1 + p)x \pm x^3. \tag{17}$$

This situation corresponds to the pitchfork case for the second iterate $\mathcal{P}^2$ map. Again consider (with $\bar{p} = 0$) the supercritical case $\mathcal{P}(x) = -(1+p)x + x^3$. As p becomes positive two fixed points of the second iterate $\mathcal{P}^2$ appear which are not fixed points of the first iterate. This means that another stable periodic orbit of period $2T$ arises whereas the original periodic orbit γ becomes unstable (see

Fig. 8). The corresponding trajectories alternate from one side of γ to the other along the direction of the eigenvector associated with the eigenvalue $\sigma = -1$. The periodic orbit is twisted around the original periodic orbit like a Möbius band. The consequence is that this bifurcation cannot occur in a 2-dimensional system since one cannot embed a Möbius band in a 2-dimensional manifold.

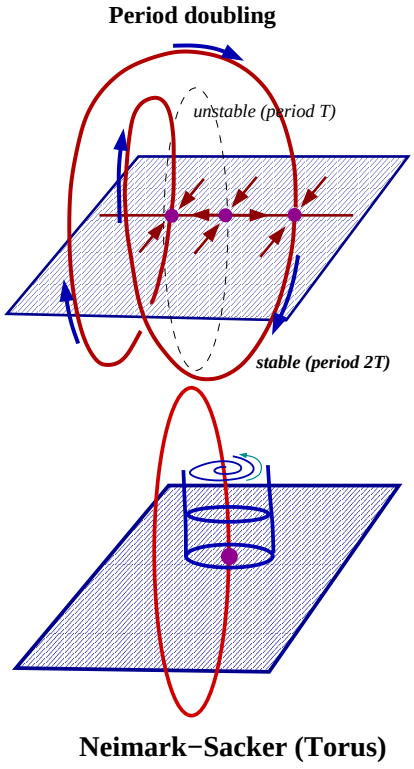

Figure 8: Phase space view of a period-doubling or flip bifurcation of a periodic orbit (upper panel) and a Neimark-Sacker or torus bifurcation (lower panel).

3. The final example corresponds to the case of a pair of complex conjugate eigenvalues $\sigma, \bar{\sigma}$ crossing the unit circle such that $|\sigma(\bar{p})| = |e^{i\varphi}| = 1$. This bifurcation is called *Neimark-Sacker* or torus bifurcation. If one assumes after reduction on a two-dimensional invariant manifold that $d\sigma(p)/dp \neq 0$ at $p = \bar{p}$ and $\sigma^j(\bar{p}) \neq 1$ for $j = 1, 2, 3, 4$ then there is a change of coordinates such that the (Poincaré) map takes the following form in polar coordinates

$$\begin{array}{l} \mathcal{P}_r(r,\theta) = r + d(p-\bar{p})r + ar^3 \\ \mathcal{P}_\theta(r,\theta) = \theta + \varphi + br^2 \end{array} . \tag{18}$$

where a, b and d are parameters. Provided $a \neq 0$, this normal form indicates that a close curve generically bifurcates from the fixed point, this closed curve

corresponds to a two-dimensional invariant torus. Note that the strong resonance cases $\sigma^j(\bar{p}) \neq 1$ for $j = 1$ and $j = 2$ correspond to the saddle-node and period-doubling bifurcations and the two other cases $j = 3, 4$ may lead to the absence of a closed curve or even several invariant curves (see [28]).

2.3 Homoclinic bifurcations of equilibria

We now discuss an important situation where there is a global change of phase space as one parameter is varied which cannot be detected by local analysis of the dynamics in the neighborhood of equilibria (or limit cycles). This situation corresponds to a *global* bifurcation and we focus here on the case of homoclinic orbits. This is a central issue in dynamical systems theory since global bifurcations in dynamical systems with $n > 2$ are in general responsible for the emergence of chaos and strange attractors. Ruelle and Takens [29] introduced the notion of a strange attractor, in referring to a chaotic attractor characterized by sensitivity to the initial state and whose dimension is fractional, rather than integer.

Homoclinic orbits correspond to the interaction between an unstable fixed point and a periodic orbit. This is exemplified by Fig. 9 which corresponds to a planar homoclinic orbit to a saddle-node fixed point. The corresponding system is

$$\begin{aligned} \dot{u} &= -u + 2v + u^2 \\ \dot{v} &= (2-p)u - v - 3u^2 + \tfrac{3}{2}uv \end{aligned} \quad . \tag{19}$$

Indeed, it can be shown that homoclinic bifurcations on the plane are determined

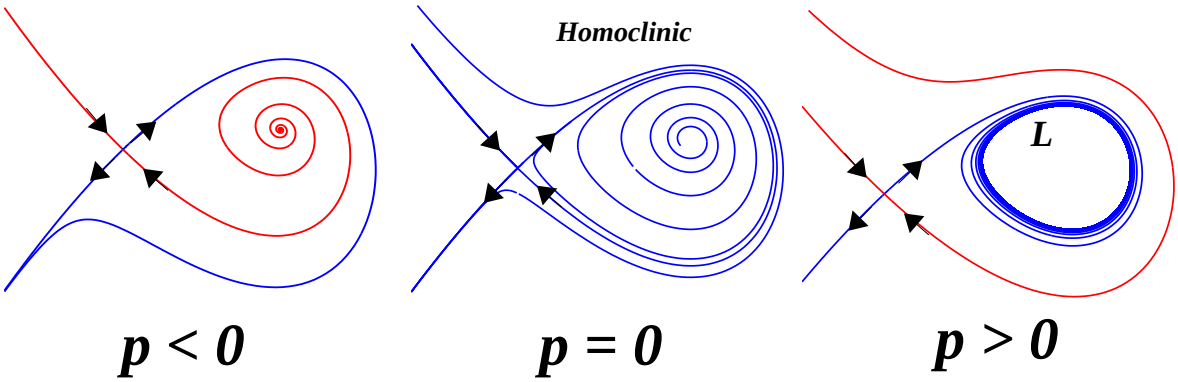

Figure 9: Phase trajectories of the system (19) in the (u, v) plane.

by the saddle quantity $\kappa = \sigma_1 + \sigma_2$, where σ_i are the eigenvalues at the (saddle-type) fixed point at the homoclinic bifurcation ($p = \bar{p}$). The system (19) corresponds to $\kappa = -2 < 0$, with $\bar{p} = 0$. As both objects connect to each other, the period of the orbit become longer as p approaches zero to become infinite at $p = 0$. The trajectory

along the unstable manifold of the fixed point approaches in infinite time the same fixed point along its stable manifold. The homoclinic orbit is then attracting the trajectories inside. For p positive, a stable periodic orbit (L in Fig. 9) is created.

Homoclinic bifurcations in systems with $n > 2$ are considerably more complicated. They most often induce stretching and folding in some bounded set of phase space and lead to the appearance of (Smale) horseshoes and possibly chaos. Typical horseshoes are given by the celebrated map sketched in Fig. 10. At the limit where this

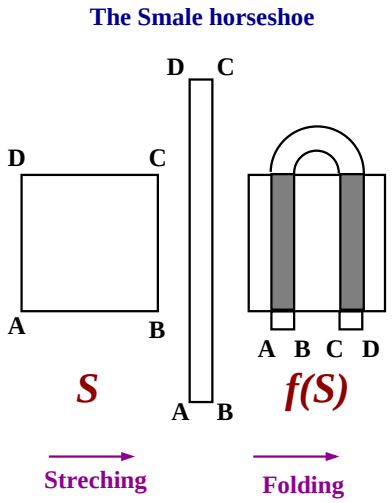

Figure 10: One iteration of the Smale map f on the square S.

map is iterated an infinite number of time, a fractal Cantor set is obtained. In the neighborhood of the saddle fixed point where the homoclinic orbit is connected, the leading eigenvalues determine how much stretching and folding occurs in phase space. In (un)favorable cases, Poincaré maps exhibit a similar iterative behavior than in the transformation (10) enabling the existence of horseshoes. In the following, we mention two important situations. Consider a three-dimensional system with two eigenvalues $\sigma_1, \sigma_2 < 0$ and one with $\sigma_3 > 0$ at the hyperbolic fixed point (saddle) and assume that homoclinic orbits exist for $p = \bar{p}$.

1. $\sigma_i \in \mathbf{R}$. In situations where there is only one homoclinic orbit, the system behaves more or less similarly to the planar case (19). In particular, a periodic orbit is created for $p \neq \bar{p}$ [30].

   The interesting case corresponds to the situation when two homoclinic orbits connect to the saddle point. In particular when there is some $\mathbb{Z}_2$ symmetry in the system it amounts to have only one parameter controlling the existence of the two homoclinic orbits at the same time. The symmetric case is of particular historical interest, since this is precisely the situation that arises in the

much studied Lorenz system [31, 32]. Under particular conditions on the eigenvalues (e.g. $-\sigma_2 < \sigma_3 < -\sigma_1$) and invariance of the system by symmetry ($(x_1, x_2, x_3) \to (-x_1, x_2, -x_3)$) one observes a *one-sided homoclinic explosion*. This means that for say $p \leq \bar{p}$ there is nothing spectacular associated with the dynamics near the broken homoclinic orbit but for $p > \bar{p}$ horseshoes appear seemingly out of nowhere. There exists a value of p, say p_0, such that for all p such that $\bar{p} < p < p_0$ the Poincaré map exhibits an invariant Cantor set (for p fixed there is only one horseshoe). An infinite number of unstable periodic orbits of all possible periods are created. Although no strange attractor actually exists, these horseshoes are considered as being the chaotic heart of numerically observed strange attractors.

We briefly illustrate the situation of the Lorenz system. This is a three-mode truncation of the Rayleigh-Bénard convection problem and corresponds to

$$\begin{aligned} \dot{x} &= s(y - x) \\ \dot{y} &= -xz + rx - y \ , \\ \dot{z} &= xz - bz \end{aligned} \tag{20}$$

with fixed parameters $s = 10, b = 10/3$ and control parameter r. As r increases, one observes the following bifurcations: for $0 < r < 1$ the origin is globally stable, at $r = 1$ there is a supercritical pitchfork bifurcation, at $r = 470/19$ there are subcritical asymmetric Hopf bifurcations and the first homoclinic explosion is observed at $r = 13.93$. It must be noted that an important bifurcation occurs at $r = 24.06...$ where the invariant Cantor set is destroyed through successive homoclinic explosions which yields to the existence of a genuine strange attractor. Note that a proof of its existence has only recently been given [33].

2. $\sigma_1 = \bar{\sigma}_2 = \rho \pm i\omega$ with $\rho < 0$ and $\sigma_3 > 0$ (saddle-focus). Let $\delta = -\rho/\sigma_3$. This case was first studied by Shilnikov [34] and the dynamics is known as the *Shilnikov phenomenon*. It can be shown that, provided $\delta < 1$, there is a finite number of fixed points (and thus periodic orbits) for $p < \bar{p}$ and $p > \bar{p}$ and a countable infinity of fixed points for $p = \bar{p}$. Thus contrary to the Lorenz bifurcation, the Shilnikov case is *two-sided*. As a matter of fact, at $p = \bar{p}$, the situation is considerably far more complicated than in the Lorenz case since there is a countable infinity of horseshoes in the neighborhood of the fixed point, each giving an infinite number of saddle fixed points. It must be noted that no symmetry is required contrary to the Lorenz case. To render the picture even more complicated, for $p \neq \bar{p}$ other homoclinic orbits appear and the Shilnikov phenomena are repeated for each of these new homoclinic orbits. We give in Fig. 11 the bifurcation behavior of the periodic orbits for the principal homoclinic orbit, such behavior is often referred to as *Shilnikov wiggles*. The reader may

find detailed proofs in [35, 25, 30]. We do not present here the case when the system possess some symmetry, it is studied in [36].

For $\delta > 1$, the situation is simple since there are no horseshoes. Only one periodic orbit exists at one side of the critical parameter value (say $p > \bar{p}$) which becomes homoclinic at $p = \bar{p}$. When a reflection symmetry is present this case is referred to as a *gluing bifurcation*.

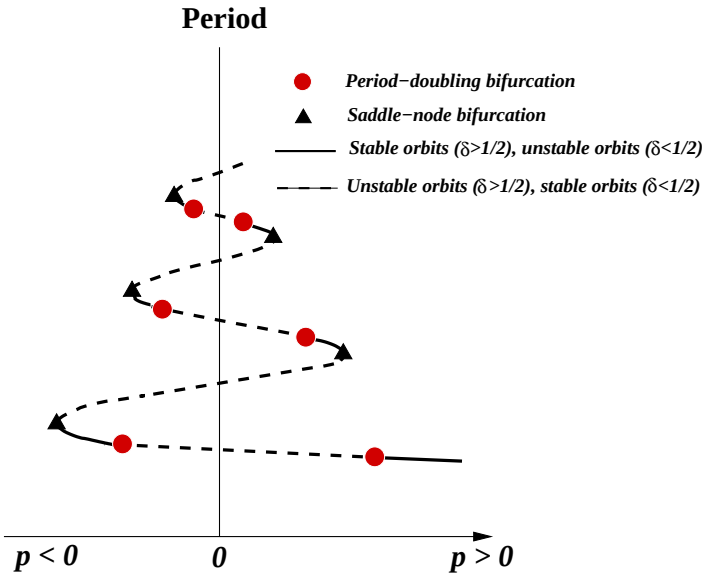

Figure 11: Dependence of the period and stability of the bifurcated periodic orbits for the case $\delta < 1$. Here the critical parameter value $\bar{p}$ is set to zero for convenience.

3 Continuation methods

The idea of continuation methods is to compute branches of steady states as one parameter is varied. It enables one to obtain meaningful and generic information on the local dynamics of a PDE model for a large range of parameter values. Although time integrations of the model are ultimately needed to detect global bifurcations as well as statistical properties of the flow, continuation methods are able to determine the first bifurcations off the branches of steady states in a rather cheap way. When interested in steady states, it naturally avoids to perform long time integrations for several values of the parameter. It is fair to say that in the context of PDEs, continuation algorithms are the same as in the context of small-dimensional dynamical systems. The difficulty rather lies on an accurate estimation of the Jacobian, the solution of the nonlinear systems of equations, and its leading eigenvalues.

The basic technique involves two main steps. The first one allows one to advance along a branch of steady states as a parameter is varied one step at a time. The second one involves a linear stability analysis of the previously computed steady state using a generalized eigenvalue solver at each step. Before going to the details, we reformulated the system (1) in the context of PDEs, namely

$$\mathcal{M}\mathbf{u}_t = -\mathcal{L}\mathbf{u} - \mathcal{N}(\mathbf{u}) + \mathcal{F}, \tag{21}$$

where $\mathbf{u}(\mathbf{x}, t) \in \mathbf{R}^n$ corresponds to a discretized solution of the original PDE, $\mathcal{M}$ is the mass matrix, $\mathcal{L}$ the discretized linear operator, $\mathcal{N}(\mathbf{u}) : \mathbf{R}^n \to \mathbf{R}^n$ the (discretized) nonlinear operator and $\mathcal{F} \in \mathbf{R}^n$ the discretized forcing term. Note that $\mathcal{M}$ is not invertible in general since we implicitly include the boundary conditions in the formulation (21). For instance, Dirichlet conditions correspond to $\mathcal{M}, \mathcal{N}(\mathbf{u})$ and $\mathcal{F}$ being zero on the boundary of the domain and $\mathcal{L}$ being the identity. Formulation (21) is thus rather general.

3.1 Pseudo-arclength methods

Finding steady states of the system (21) amounts to solve

$$\Phi(\mathbf{u}, p) = 0, \text{ where } \Phi(\mathbf{u}, p) = \mathcal{L}\mathbf{u} + \mathcal{N}(\mathbf{u}) - \mathcal{F}. \tag{22}$$

Pseudo-arclength methods [37, 38] are very often used. The idea is to parametrize branches of solutions $\Gamma(s) \equiv (\mathbf{u}(s), p(s))$ with an arclength parameter s (or an approximation of it, thus the term 'pseudo') and choose this parameter as the continuation parameter instead of p. An additional equation is obtained by approximating the normalization condition of the tangent $(\dot{\mathbf{u}}(s), \dot{p}(s)) \equiv \dot{\Gamma}(s)$ to the branch $\Gamma(s)$, where the dot refers to the derivative with respect to s, namely $|\dot{\Gamma}|^2 = 1$. This condition is approximated by

$$\dot{\mathbf{u}}_0^T(\mathbf{u} - \mathbf{u_0}) + \dot{p}_0(p - p_0) - \Delta s = 0, \tag{23}$$

where $(\mathbf{u}_0, p_0)$ is a known starting solution (or a previously computed point) on a particular branch and Δs is the (small) steplength. In order to compute the tangent $\dot{\Gamma}_0(s)$, one differentiates $\Phi(\mathbf{u}(\mathbf{s}), p(s)) = 0$ with respect to s at $(\mathbf{u}_0, p_0)$ to find

$$\left[\Phi_{\mathbf{u}}^0, \Phi_p^0\right] \dot{\Gamma}_0(s) = \begin{pmatrix} \frac{\partial \Phi_1^0}{\partial u_1} & \cdots & \frac{\partial \Phi_1^0}{\partial u_n} & \frac{\partial \Phi_1^0}{\partial p} \\ & & & \\ \frac{\partial \Phi_n^0}{\partial u_1} & \cdots & \frac{\partial \Phi_n^0}{\partial u_n} & \frac{\partial \Phi_n^0}{\partial p} \end{pmatrix} \dot{\Gamma}_0(s) = 0, \tag{24}$$

where $\Phi_{\mathbf{u}}^0$ and Φ_p^0 correspond to the derivatives evaluated at $(\mathbf{u}_0, p_0)$. If $(\mathbf{u}_0, p_0)$ is not a bifurcation point, then dim ker $\left[\Phi_{\mathbf{u}}^0, \Phi_p^0\right] = 1$ and therefore $\left[\Phi_{\mathbf{u}}^0, \Phi_p^0\right]$ has rank n. We

may thus determine $\dot{\Gamma}_0(s)$ as the null vector of the $n \times (n+1)$ matrix $[\Phi_{\mathbf{u}}, \Phi_p]$. In practice, this can be done by upper triangulating the matrix $[\Phi_{\mathbf{u}}, \Phi_p]$ and solving a $(n+1)\times(n+1)$ extended system with a one in the right-lower corner and right-hand side. Then the normalization condition $|\dot{\Gamma}_0|^2 = 1$ is used. A *predictor* solution of (23) is given by

$$\begin{array}{lllll} \mathbf{u} = & \mathbf{u_0} & +\Delta s & \dot{\mathbf{u}}_0 \\ p = & p_0 & +\Delta s & \dot{p}_0 \end{array} . \tag{25}$$

The next step is then to project the predictor solution $(\mathbf{u}, p)$ back onto the branch in a direction orthogonal to the tangent $\dot{\Gamma}_0$. This is called the *corrector* algorithm. It should rely on a robust nonlinear solver for the system (22). The one of common use is the Newton-Raphson method. This method has a quadratic convergence provided the initial starting solution is close enough to the solution. The *predictor* step just does that, all the more so as Δs is small. The initial guess will thus be the predictor solution (25). Newton-Raphson iterations with iteration index k, can then be written as

$$\begin{pmatrix} \Phi_{\mathbf{u}}(\mathbf{u}^k, p^k) & \Phi_p(\mathbf{u}^k, p^k) \\ \\ \dot{\mathbf{u}}_0^T & \dot{p}_0 \end{pmatrix} \begin{pmatrix} \Delta\mathbf{u}^{k+1} \\ \\ \Delta p^{k+1} \end{pmatrix} = \begin{pmatrix} -\Phi(\mathbf{u}^k, p^k) \\ \\ r_{n+1} \end{pmatrix} . \tag{26}$$

where $r_{n+1} = \Delta s - \dot{\mathbf{u}}_0^T(\mathbf{u}^k - \mathbf{u_0}) - \dot{p}_0(p^k - p_0)$.

Once $(\Delta\mathbf{u}^{k+1}, \Delta p^{k+1})$ is found, one sets

$$\begin{array}{ll} \mathbf{u}^{k+1} = & \mathbf{u}^k + \Delta\mathbf{u}^{k+1} \\ p^{k+1} = & p^k + \Delta p^{k+1} \end{array} . \tag{27}$$

In practical situations, it is better to solve two $n \times n$ linear systems instead of solving directly (26), namely

$$\begin{array}{ll} \Phi_{\mathbf{u}}(\mathbf{u}^k, p^k)\mathbf{z}_1 = & -\Phi(\mathbf{u}^k, p^k) \\ \Phi_{\mathbf{u}}(\mathbf{u}^k, p^k)\mathbf{z}_2 = & \Phi_p(\mathbf{u}^k, p^k) \end{array} . \tag{28}$$

Then, the solution of (26) is

$$\Delta p^{k+1} = \frac{r_{n+1} - \dot{\mathbf{u}}_0^T\mathbf{z}_1}{\dot{p}_0 - \dot{\mathbf{u}}_0^T\mathbf{z}_2}, \text{ and } \Delta\mathbf{u}^{k+1} = \mathbf{z}_1 - \Delta p^{k+1}\mathbf{z}_2. \tag{29}$$

The method is illustrated geometrically by Fig. 12. It must be noted that pseudo-arclength methods rely essentially on a correct estimation of the Jacobian matrix $[\Phi_{\mathbf{u}}, \Phi_p]$, and this can be done in at least two ways: explicitly 'by hand' or numerically using the approximation $\Phi_x \simeq (\Phi(x+\epsilon) - \Phi(x))/\epsilon$ for small ϵ. It is usually faster to do it 'by hand' provided one is cautious in treating the boundary conditions. Failure to do so in general prevents the Newton-Raphson method to converge quadratically.

The advantage of pseudo-arclength methods over traditional continuation methods is that the Jacobian of the extended system $[\Phi_{\mathbf{u}}, \Phi_p]$ has rank n even at saddle-node

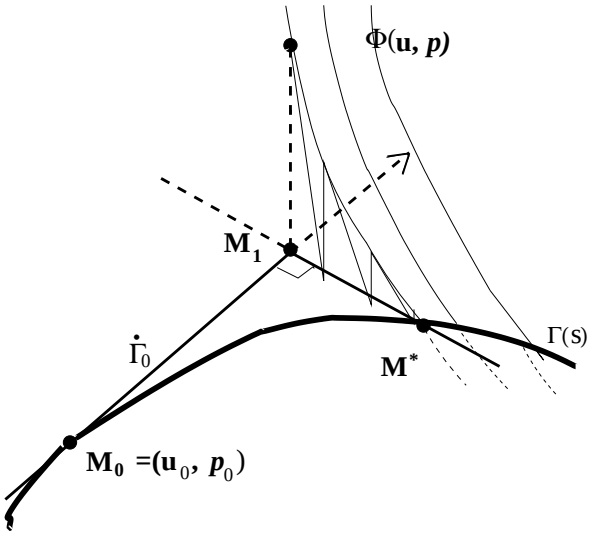

Figure 12: Sketch of the pseudo-arclength method.

points where $\Phi_{\mathbf{u}}$ becomes singular. Hence, one can easily continue around saddle-node bifurcation as illustrated in Fig. 13. One other advantage is that it allows to compute branches of unstable as well as stable solutions.

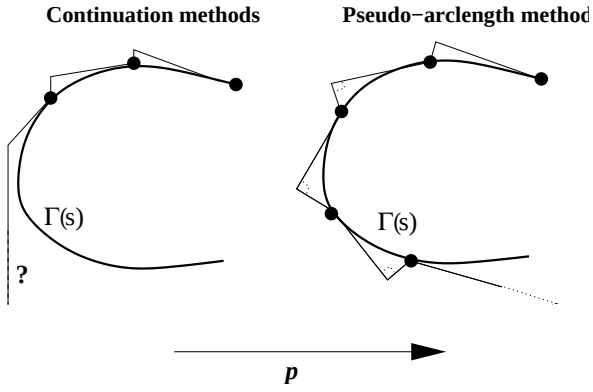

Figure 13: Pseudo-arclength methods can go through saddle-node bifurcation. The direction of continuation is to the left, that is, toward decreasing values of p.

3.2 Linear stability problem

In order to detect bifurcations of the steady states $(\bar{\mathbf{u}}, \bar{p})$ which have been previously computed by a pseudo-arclength method, one sets first $\mathbf{u} = \bar{\mathbf{u}} + \mathbf{v}$ in (21) to yield the

linearized (discretized) PDE:

$$\mathcal{M}\mathbf{v}_t = -\mathcal{L}\mathbf{v} - \mathcal{N}_{\mathbf{u}}(\bar{\mathbf{u}})\mathbf{v}. \tag{30}$$

We look for solutions in the form $\mathbf{v} = \hat{\mathbf{v}}\mathrm{e}^{\sigma t}$ so that one obtains the generalized eigenvalue problem:

$$\mathcal{A}\hat{\mathbf{v}} = \sigma\mathcal{B}\hat{\mathbf{v}}, \text{ with } \mathcal{A} = \mathcal{L} + \mathcal{N}_{\mathbf{u}}(\bar{\mathbf{u}}) \text{ and } \mathcal{B} = -\mathcal{M}. \tag{31}$$

The matrix $\mathcal{B}$ is usually singular due to the presence of (time-independent) boundary conditions and indeed whenever time derivatives are absent from the original PDE system. Like in the traditional approach presented in the section 2, one is mostly interested in eigenvalues σ which cross the imaginary axis. The eigenvalues closest to the imaginary axis are often called *leading* eigenvalues. When n is very large, it is not possible to compute all the eigenvalues of the system (31) and one must rely on more sophisticated methods which are able to compute the leading ones. We present here a very efficient method called the Simultaneous Iteration Technique (SIT) [39].

The idea is to apply a transformation mapping of the left complex half plane into the unit disk so that complex eigenvalues crossing the imaginary axis are transformed into complex eigenvalues leaving the unit disk. The complex transformation is

$$z \to z' = \frac{a - b + z}{a + b - z}, \ b \in \mathbf{R}, a > 0. \tag{32}$$

It is easy to check that for $\mathcal{R}e\ z \leq b$ one has $|z'| \leq 1$. The parameter b shifts the spectrum along the real axis, whereas the parameter a stretches it. One then applies the transformation (32) to the generalized eigenvalue problem (31) to obtain

$$\mathcal{D}^{-1}\mathcal{C}\hat{\mathbf{v}} = \lambda\hat{\mathbf{v}}, \text{ where } \lambda = \frac{a - b + \sigma}{a + b - \sigma}, \text{ and } \begin{array}{ll} \mathcal{C} = & \mathcal{A} + (a - b)\mathcal{B} \\ \mathcal{D} = & -\mathcal{A} + (a + b)\mathcal{B} \end{array}. \tag{33}$$

Although the matrix $\mathcal{B}$ is in general singular, the matrices $\mathcal{D}$ and $\mathcal{C}$ are generically not singular. The new eigenvalue problem (33) can then be treated using generalized power methods which compute the eigenvalues with the largest absolute values [40]. Another technique used to solve the generalized eigenvalue problems is the Jacobi-Davidson QZ method [41]. In this method a Krylov subspace of $\mathbf{R}^n$ is constructed and special projection techniques are used to find the eigenvalues and eigenvectors.

3.3 Branch switching and homotopy methods

Although a linear stability analysis is aimed at detecting the bifurcations, it does not provide a way to compute the new branches of solutions which appear at the bifurcations. There are traditionally at least two ways to switch on branches of steady

states when det Φ_u in (26) changes sign but $\dot{p}$ does not, namely for transcritical and pitchfork bifurcations. Let the tangent to the original branch be denoted by $(\dot{\mathbf{u}}_0, \dot{p}_0)$ and the solution at the bifurcation $(\mathbf{u}^\star, p^\star)$.

The first method consists in computing a vector $(\hat{\mathbf{u}}, \hat{p})$ which belongs to the plane spanned by $(\dot{\mathbf{u}}_0, \dot{p}_0)$ and the tangent to the new branch, and which is orthogonal to $(\dot{\mathbf{u}}_0, \dot{p}_0)$. It exactly amounts to solve the system

$$\begin{pmatrix} \Phi_{\mathbf{u}}(\mathbf{u}^\star, p^\star) & \Phi_p(\mathbf{u}^\star, p^\star) \\ \dot{\mathbf{u}}_0{}^T & \dot{p}_0 \end{pmatrix} \begin{pmatrix} \hat{\mathbf{u}} \\ \hat{p} \end{pmatrix} = \begin{pmatrix} \mathbf{0} \\ 0 \end{pmatrix}. \tag{34}$$

The first equation $\Phi_{\mathbf{u}}\hat{\mathbf{u}} + \Phi_p\hat{p} = 0$ indeed insures that $(\hat{\mathbf{u}}, \hat{p})$ belongs to the plane spanned by the two tangent vectors since $\Phi_{\mathbf{u}}$ has a nontrivial kernel at the bifurcation point. The solution to (34) is easily determined to be

$$\hat{p} = \frac{-\mathbf{u}_0^T \phi}{\dot{p}_0 - \dot{\mathbf{u}}_0^T \mathbf{z}}, \ \hat{\mathbf{u}} = \phi - \hat{p}\mathbf{z}, \tag{35}$$

where ϕ is a null vector of $\Phi_{\mathbf{u}}(\mathbf{u}^\star, p^\star)$ and $\mathbf{z}$ is the solution of $\Phi_{\mathbf{u}}(\mathbf{u}^\star, p^\star)\mathbf{z} = \Phi_p(\mathbf{u}^\star, p^\star)$. In practice, the null vector is calculated by inverse iteration [42] or a good approximation of it may be given by the null eigenvector obtained by the linear stability analysis. To determine a point on the new branch, the Newton process is started with the *predictor*

$$\mathbf{u} = \mathbf{u}^\star \pm \Delta s \ \hat{\mathbf{u}}; p = p^\star \pm \Delta s \ \hat{p}, \tag{36}$$

where the $\pm$ indicates that solutions can be found on either side of the known branch.

The other method consists in using an homotopy parameter θ that perturbs the original problem to a problem where only saddle-node bifurcations are observed. As stated in section 2, pitchfork and transcritical bifurcations can always be perturbed to give saddle-node bifurcations. The method is illustrated for the case of the pitchfork bifurcation in Fig. 14. One is starting from the solution a and wants to reach either the solution b or c. The idea is simply to compute the branch of solutions along the direction θ which corresponds here to a parameter which perturbs the problem symmetry (for instance the forcing term in Eq. (21)). The bifurcation diagram for $\theta = \theta^\star \neq 0$ is given to have an idea of the two-dimensional set of solutions. Homotopy methods are very powerful and can even solve more complicated problems like finding isolated branches of solutions in nontrivial systems.

3.4 Continuation of periodic orbits

We now turn to the numerical computation of stable and unstable periodic orbits versus a parameter p of autonomous problems. There are basically two methods to compute periodic orbits: one method directly solves a boundary value problem while in the other method, fixed points of the Poincaré map are computed.

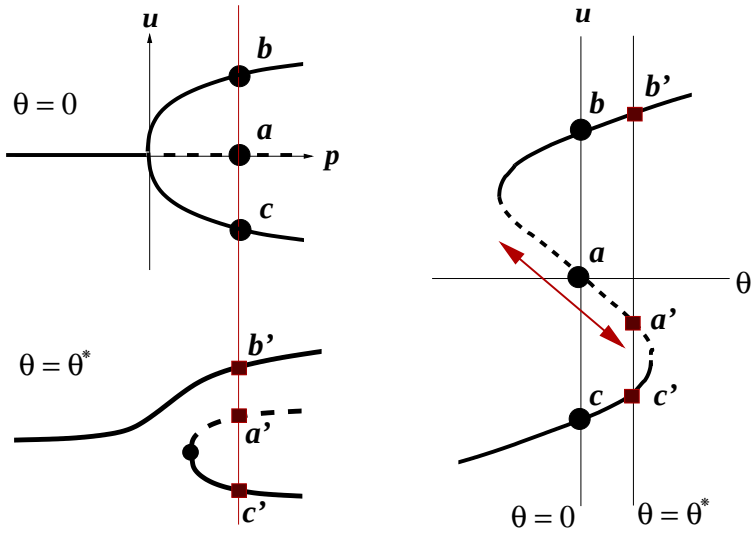

Figure 14: Use of homotopy methods to compute branch switching. The left panels correspond to the bifurcation diagrams when varying p for two different values of the perturbation homotopy parameter θ, the right panel is a cross-section of the right panels at constant p corresponding to the thin red line. One initially starts from the fixed point a and follows the branch along the homotopy parameter θ (left panel).

3.4.1 Boundary value problem approach

As the period T has an a priori unknown dependence on p, time is usually rescaled as $\tilde{t} = t/T$, such that the original problem (1) transforms into

$$\frac{d\mathbf{x}}{dt} = T\mathbf{f}(\mathbf{x}, \mathbf{p}). \tag{37}$$

where $t \in [0, 1]$. The computation of a periodic orbit of (37) can be considered as a boundary value problem in time, since $\mathbf{x}(0) = \mathbf{x}(1)$. For autonomous systems, these boundary conditions do not fully determine the orbit since its phase can be freely shifted. Hence, in a pseudo-arclength methods we need, in addition to the parametrizing equation, also a normalization of the phase, i.e., a phase condition.

Suppose we have determined a periodic solution $(\mathbf{x}^0, T^0)$ at $p = p^0$, then many methods solve the problem (37) with

$$\int_0^1 (\mathbf{x}(t) - \mathbf{x}^0(t))^T \dot{\mathbf{x}}^0(t) dt \quad + \quad (T - T^0)\dot{T}^0 + (p - p^0)\dot{p}^0 = \Delta s \tag{38a}$$

$$\int_0^1 \mathbf{x}^T(t)\dot{\mathbf{x}}^0(t) dt \quad = \quad 0 \tag{38b}$$

$$\mathbf{x}(0) \quad = \quad \mathbf{x}(1) \tag{38c}$$

where Δs is again the step length. The phase condition (38b) is obtained by requiring that the distance between the new and the old periodic solution is minimized with respect to the phase. The problem (38) is solved either by so-called single- or multiple shooting techniques or by collocation techniques. A starting point of the periodic orbit can usually be obtained by a perturbation analysis near a Hopf bifurcation.

3.4.2 Fixed points of the Poincaré map

In this approach, we first have to define a Poincaré section which is transversal to the flow. This can be done by defining a hyperplane Σ as

$$g(\mathbf{x}) = \mathbf{n}.(\mathbf{x} - \mathbf{x}_*) \tag{39}$$

where $\mathbf{n}$ is the normal to the hyperplane and $\mathbf{x}_*$ a certain point in Σ. In practice, one can often take intersections with one of the coordinate planes. The Poincaré map on Σ is defined as

$$\mathcal{P}(\mathbf{x}, p) = \phi(t(\mathbf{x}), \mathbf{x}, p) \tag{40}$$

where ϕ is a solution of (1). Here, $t(\mathbf{x})$ is the return time and $sign(\mathbf{n}.\phi(0, \mathbf{x}, p)) = sign(\mathbf{n}.\phi(t(\mathbf{x}), \mathbf{x}, p))$ such that the orbit intersects Σ with the same orientation at both times.

Periodic orbits are computed from

$$\mathbf{x} - \mathcal{P}(\mathbf{x}, p) = 0 \tag{41}$$

with $\mathbf{x} \in \Sigma$. In practice, the Poincaré section is parametrized and, leaving out this detail, the solutions of (41) versus the parameter p are again calculated by the pseudo-arclength method. This leads to systems of equations (26) where the Jacobian matrix is now given by $I - \mathcal{P}_x(\mathbf{x}^k, p^k)$. The additional difficulty is now that we do not want to construct the Poincaré map explicitly.

If we solve the linear systems (28) with an iterative method, however, we need only the result of a product of the Jacobian with a vector, say $\mathbf{v}$. Thereto, we need to perform two transient integrations, one with the full system (1) and one with the first variational equation (13). If $\mathbf{x}^k$ is again the k^{th} iterate of the Newton-Raphson process, then the initial conditions of the full system are $\mathbf{x}^k + \mathbf{v}$, while for the variational equation, the initial conditions are $\mathbf{v}$. Integration of (28) until an intersection with Σ provides the vector $\mathbf{x}^*$, while integration of (13) provides $\mathbf{y}^*$. It can be shown that in this case

$$P_x\mathbf{v} = \mathbf{y}^* - \mathbf{z}^* \frac{\mathbf{n}.\mathbf{y}^*}{\mathbf{n}.\mathbf{z}^*} \tag{42}$$

where $\mathbf{z}^* = \mathbf{f}(\mathbf{x}^*, p)$. A more detailed description of this algorithm in the context of PDEs can be found in [43].

3.5 Application potential

The early and best-known applications of continuation methods to atmospheric and ocean dynamics involved a very small number of degrees of freedom [31, 44, 45, 46]. For instance, the Lorenz model (20) is probably one of the most studied dynamical system of the past forty years. As dynamical systems theory is being rapidly extended to infinite-dimensional systems governed by PDEs [18], the applications to atmospheric, oceanic and climate dynamics are becoming more and more sophisticated [19, 8]. Indeed, the computer power available to study bifurcation sequences is increasing rapidly so that more sophisticated numerical methods can be applied.

In the mid-1970s, it was possible to compute the first one or two bifurcations for spatially 1-D energy balance models with [47, 48, 49] or without [50] spectral truncation. In the mid-1980s, truncations to tens of degrees-of-freedom of 2-D geophysical flow problems could be approached in this manner [19]. In particular, continuation methods were first seen in the seminal paper of Legras and Ghil on atmospheric flow regimes [51]. In the last few years, there has been a spectacular increase of bifurcation studies involving a large number of degrees of freedom. For instance, bifurcation sequences have been computed for 2-D oceanic flows [9, 10, 11, 52, 53, 54, 55, 56] as well as 3-D flows [57, 2, 58, 59]. All these studies involved tens of thousands of degrees-of-freedom with the noticeable exception of [59] which involved about 300 000 degrees of freedom. Simplified atmospheric, oceanic or coupled GCMs have thus become amenable to a systematic study of their large-scale variability.

The applicability strongly depends on the availability of efficient solvers for the linear systems arising from the Newton-Raphson method. Recently, the development of targeted solvers for ocean models [60, 61,] has opened the way to tackle problems with up to 10^6 degrees of freedom. The latest solver is based on a block Gauss-Seidel preconditioner, which uses the special structure and properties of the hydrostatic and geostrophic balances.

4 Application to the wind-driven ocean circulation

One of the central problems of physical oceanography is to understand the physics of the near-surface ocean circulation at midlatitudes. The North-Atlantic circulation is composed of two large-scale gyres, namely a subpolar cyclonic and a subtropical anticyclonic gyre associated with a well-known eastward jet, the Gulf Stream. These two cyclonic and anticyclonic gyres and the associated intense zonal jet are essentially driven by the mid-latitude easterlies and trade winds in the northern hemisphere. This system is referred to as the *wind-driven double-gyre circulation*. Figure 15 gives a schematic representation of this circulation in the Gulf stream region.

The Kuroshio extension is another example of a double-gyre system in the North

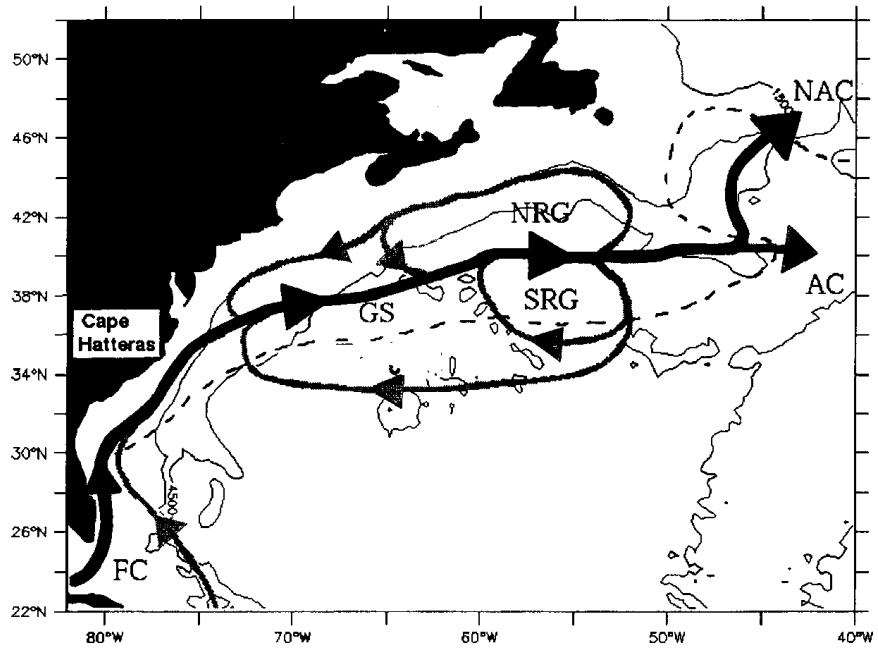

Figure 15: Sketch of the near-surface circulation in the Gulf Stream region. Bold lines: Florida current (FC) and Gulf Stream (GS), branching into the North Atlantic Current (NAC) and Azores Current (AC). The abbreviations NRG and SRG indicate Northern (cyclonic) and Southern (anticyclonic) recirculation gyre, respectively (from [62]).

Pacific. Similar systems exist in the Southern hemisphere as well such as the Brazil and Malvinas currents in the South Atlantic. These intense oceanic currents exhibit highly complex multi-scale spatio-temporal structures. Spatial scales from several km (eddies, rings) up to hundred km (meanders, recirculation gyres) are associated with time scales of months to decades.

The fundamental question is to understand the origin of the low-frequency variability of the double-gyre wind-driven circulation. This low-frequency variability involves timescales of several years to several decades. Although the atmosphere above the mid-latitude oceans is highly variable, some low-frequency phenomena may be intrinsically caused by nonlinear oceanic dynamical processes. In the following, we describe how the use of dynamical systems and bifurcation theory enables one to achieve a rather deep understanding in this particular problem. In particular, we will demonstrate that low-frequency variability can have a sole internal origin and that it is related to instabilities of the mean flow.

4.1 The double-gyre quasi-geostrophic model

Quasi-geostrophic (QG) equations are very often used in ocean- and atmosphere studies. They provide a rather simple 2-D model which describes qualitatively the behavior of geophysical flows at mid-latitudes. In the context of the double-gyre wind-driven circulation, these equations read

$$\begin{aligned} & q_t + [\psi_x q_y - \psi_y q_x] + \beta\psi_x - \nu\Delta^2\psi = -\mu\Delta\psi - \alpha\sin(2\pi y/L_y) \\ & q = \Delta\psi - \lambda_R^{-2}\psi \end{aligned} \quad , \tag{43}$$

where x denotes the longitudinal direction and y the latitudinal one on a rectangular domain $\Omega = (0, L_x) \times (0, L_y)$. These equations are indeed very similar to the incompressible 2-D Navier-Stokes equations expressed in vorticity form, in particular the velocities are related to the streamfunction ψ by $u = -\psi_y$ and $v = \psi_x$ and q is called here the potential vorticity. The RHS of (43) comes from the vertical integration of the fluid layer from bottom to surface. It is composed of $-\mu\Delta\psi$, the stress at the bottom which is proportional to the vorticity, and the wind stress at the surface $\alpha\sin(2\pi y/L_y)$ which is prescribed and time-independent. The eddy-viscosity operator $\nu\Delta^2\psi$ plays a rather different role and is needed here as a turbulent closure in order to stop the enstrophy cascade toward the small scales. The term $\beta\psi_x$ is of paramount importance since it represents the variation of the Coriolis force on a β plane. Indeed, on such a plane, the Coriolis parameter f is assumed to be equal to $f = f_0 + \beta y$. Note that it is rather the variations of f with latitude which are important and permit the propagation of the so-called Rossby waves [63].

The equations (43) describe the dynamics of flows which are in geostrophic equilibrium, i.e. when there is a balance between Coriolis and pressure forces so that

the ocean or atmospheric fluid parcels flow along the direction of lines of constant pressure. The boundary conditions can either be no-slip ($\psi = \partial\psi/\partial\mathbf{n} = 0$) or free-slip ($\psi = \Delta\psi = 0$) although more accurate boundary conditions can also be used [64]. The sinusoidal forcing term corresponds to the curl of the wind-stress field, namely easterlies in the northern and southern part of the basin and westerlies in the middle. It is assumed here that the forcing term obeys some symmetry and in particular that the amounts of negative and positive vorticity due to the winds are equal. This choice implies that the model (43) is invariant with respect to the $\mathbb{Z}_2$ (reflection) symmetry

$$\mathcal{S}\psi(x, y) = -\psi(x, L_y - y). \tag{44}$$

This property is important since one wants to start from the most idealized picture where the system has the largest number of symmetries and then perturb it when proceeding along the axis of complexity (see Fig. 1).

Figure 16 shows a typical bifurcation diagram of the double-gyre circulation in small oceanic basins [65]. This diagram is obtained using a pseudo-arclength method with linear stability analysis as described in section 3. Three distinct branches of steady solutions are obtained. The first branch is characterized by perfectly antisymmetric solutions ψ for which $\mathcal{S}\psi = \psi$. After the first saddle-node bifurcation point L these solutions become inertially dominated, the flows become very energetic and the recirculation gyres eventually fill the entire basin. Two pitchfork bifurcations (see Fig. 4 in section 3) P_1 and P_2 occur on the antisymmetric branch. They are responsible for the appearance of asymmetric solutions, say ψ_1 and ψ_2, which are conjugated to each other, that is $\mathcal{S}\psi_1 = \psi_2$. The second pitchfork bifurcation at P_2 leads to a branch of asymmetric flows with their jet aligned in the west-east direction and a confluence point either shifted to the south or to the north of the mid-axis of the basin. The flows on the two branches starting from P_1 exhibit meandering of the jet downstream of the recirculation dipole (see details in [66]), with either a stronger subtropical gyre (upper branch) or a stronger subpolar gyre (lower branch). The weaker gyre is more affected by the asymmetry and wraps around the stronger one. Hopf bifurcations $H_1, H_{\text{gyre}}, H_3$ are detected along these asymmetric branches indicating that the steady states are destabilized by successive oscillatory instabilities.

The path of the real part of the leading eigenvalues and associated eigenvectors of (31) is shown in the Fig. 17. The connection between this figure and Fig. 16 is simple: instead of showing the quantity $\Psi_{\text{subtropical}}$ along the various branches of steady states, one plots instead the real and imaginary parts of the leading eigenvalue of the linearized equation. These paths are found by solving (31) at each step of the continuation algorithm. One thus observes the crossing of the imaginary part in the complex plane by real eigenvalues (thick curves) giving the saddle-node and the two pitchfork bifurcations as seen previously in Fig. 16. As expected, the streamfunction patterns are symmetric for the case of the pitchfork bifurcation and antisymmetric for the case of the saddle-node bifurcation. The important thing about Fig. 31 however is

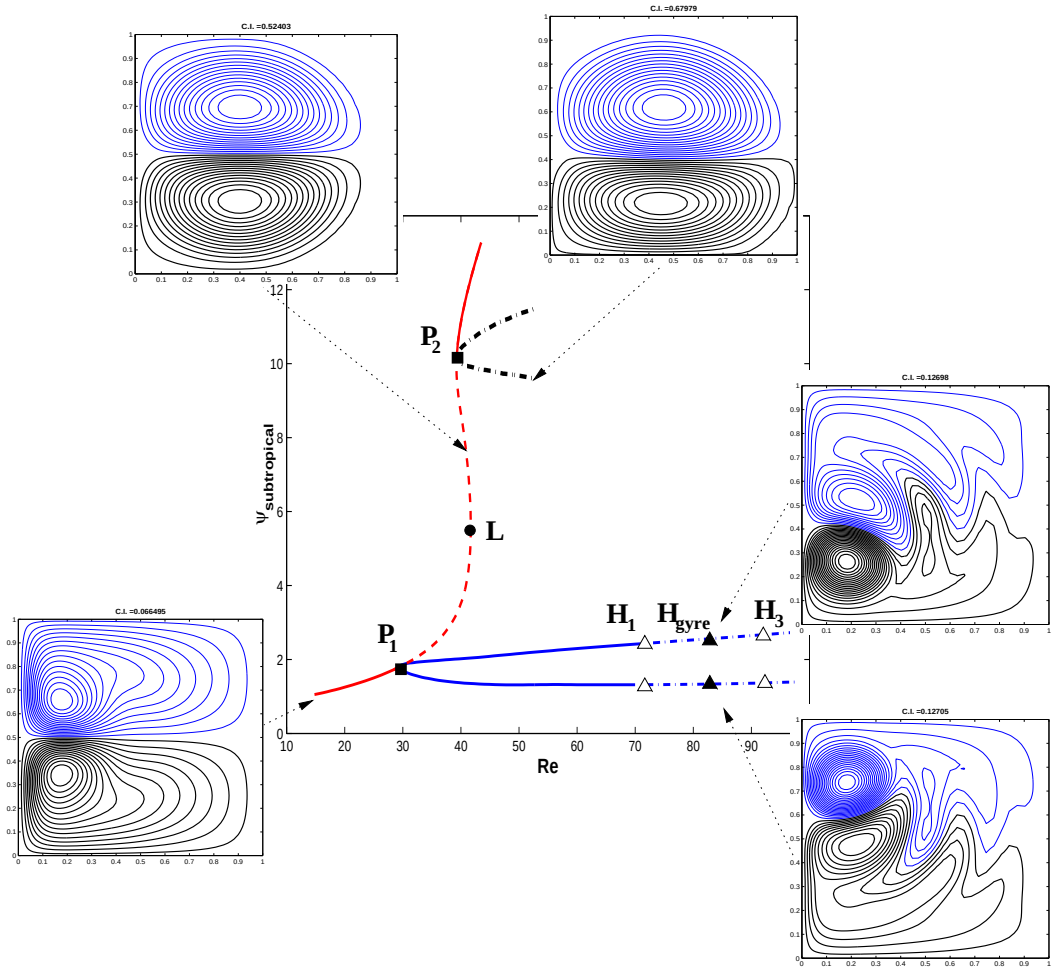

Figure 16: Bifurcation diagram for the QG model (43). Here, the maximum value of the streamfunction of the subtropical gyre ($\Psi_{\text{subtropical}}$) is plotted versus the Reynold number $Re = UL_x/\nu$, where U is a typical characteristic horizontal velocity. The bifurcations P_1, P_2 correspond to the pitchfork bifurcations (squares), whereas the triangles indicate the location of the Hopf bifurcations. The saddle-node bifurcation L is indicated by a dot. The panels correspond to the upper-layer streamfunctions, positive contours are represented by thick lines, negative contours by thin lines together with contour intervals (from [65]).

the remarkable mode-merging observed at M where the two real eigenvalues become complex conjugated. Although it corresponds to a topological change of behavior in phase space, it is not rigorously speaking a bifurcation since, at M, the oscillatory behavior is damped. Nevertheless, this oscillatory eigenmode is eventually destabilized at $H_{\rm gyre}$ in Fig. 16 through a Hopf bifurcation. It should be clear from the lower panel of Fig. 17 that the imaginary part of the eigenvalue is growing quadratically and thus leads to an oscillatory instability of rather low frequency compared to other complex eigenvalues in the spectrum. This merging phenomenon is as generic as the pitchfork bifurcation P_1 and is seen in much more complex situations and models [55, 67].

This remarkable result is indeed one of the starting points of a much deeper understanding of the low-frequency dynamics of the double-gyre circulation in the recent years. To start with, the mode referred to as *gyre mode* in Fig. 17 was already known since the work of [6] on a shallow-water version of the model (43). Its particular spatial structure induces a relaxation oscillation of the gyres associated with periods of several years. These relaxation oscillations moreover become chaotic in strongly nonlinear regimes. For a long time, the origin of such modes was unexplained. Indeed, they appeared seemingly from nowhere and contrary to most of the other instabilities found (e.g. Hopf bifurcations H_1 and H_3 in Fig. 16) linear theories of the double-gyre flow cannot explain their existence, as it appears that this phenomenon is essentially nonlinear. This result illustrates the power of dynamical systems and bifurcation theory.

At the same time, some authors [53, 20, 66] argued that the chaos observed in more nonlinear regimes could not be the result of several competing instabilities interacting according to the Ruelle-Takens route to chaos [68]. They suggested the presence of a global homoclinic (or possibly heteroclinic) bifurcation in the model (43). It is only recently that such a bifurcation has been explicitly detected [21, 55, 16]. The connection with the gyre modes is also clearly established in [55, 16]: these modes span larger and larger regions of phase space as the nonlinearity of the model increases and form a symmetric homoclinic orbit later on. This is illustrated by Fig. 18 where the unfolding of the limit cycles a, b, c and d for a parameter approaching the critical value at the symmetric homoclinic bifurcation is clearly seen.

Note that in this case, a poor man's continuation method of periodic orbits was used, that is, several time integrations for particularly well-chosen parameters near the critical value were achieved. It is also possible using continuation techniques to have some ideas about the nature of the homoclinic bifurcation by computing the leading eigenvalues at the hyperbolic fixed point to which the homoclinic cycle is connected. This is illustrated by Fig. 19 which provides a loci of pitchfork, homoclinic and saddle-node bifurcations in the 2-parameter plane spanned by the wind-stress intensity α and lateral viscosity ν (see Eq. (43)). Figure 20 corresponds to the linear stability analysis at the hyperbolic point where the homoclinic orbit is connected.

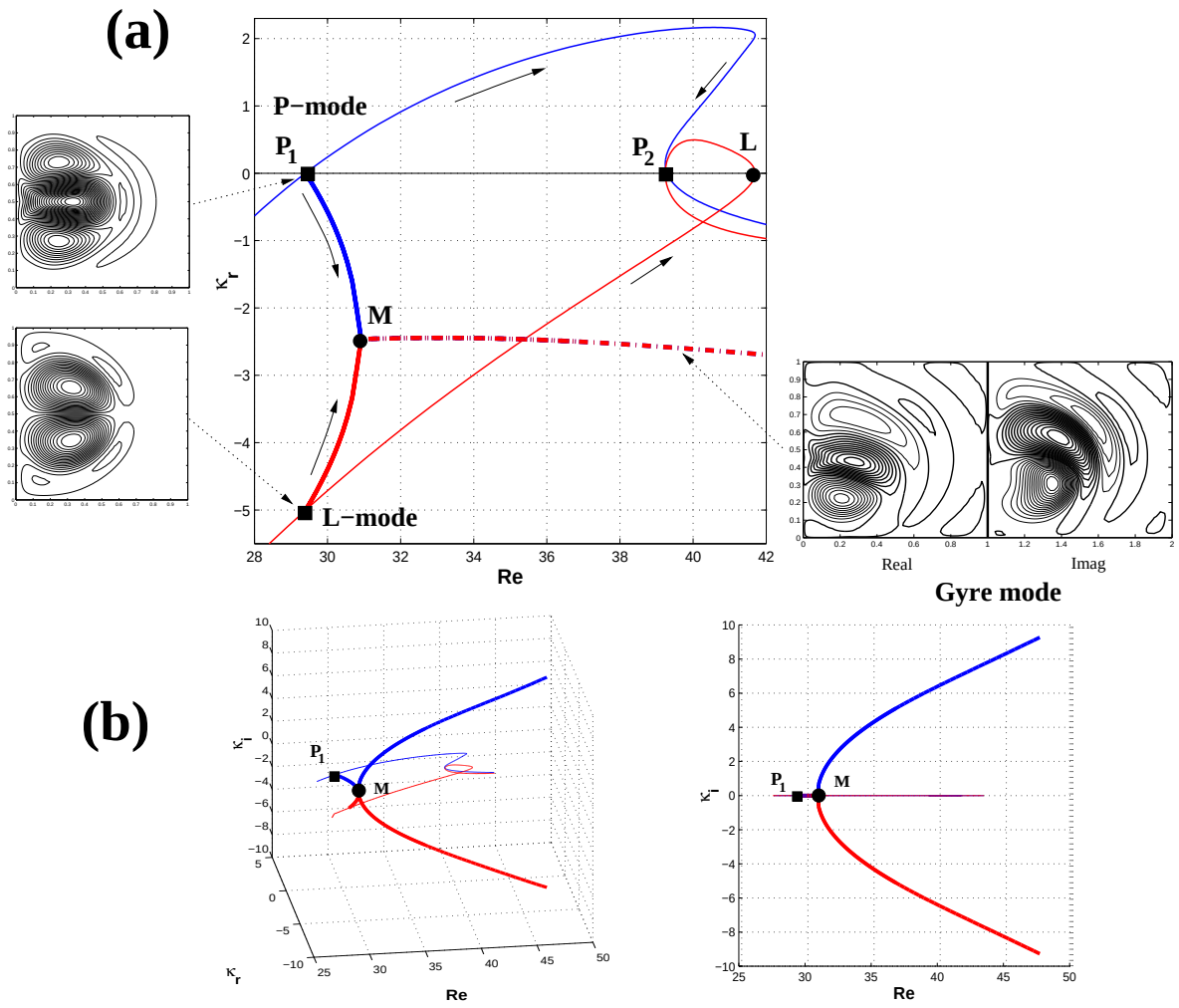

Figure 17: Spectral behavior of the eigenmodes involved into the various bifurcations off the antisymmetric branch for the barotropic QG model shown in red and blue in Fig. 16. The real part, panel (a), and imaginary part, panel (b), of the P-mode and L-mode eigenvalues are plotted versus Re. Thick lines, beginning at P_1 in Fig. 16 and ending at M, corresponds to the path of these two modes on the asymmetric branch, thin lines to the path on the antisymmetric branch. The dash-dot thick line indicates a non-zero imaginary part. At M, the merging between the P-mode and L-mode occurs. The various panels show the streamfunction patterns at the locations indicated by the arrows (from [65]).

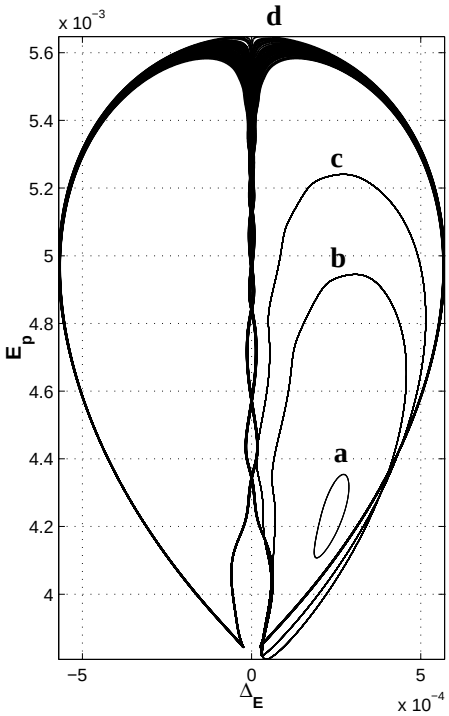

Figure 18: Unfolding of the relaxation oscillations induced by the gyre modes in the planed spanned by the total potential energy E_p versus $\Delta_E = E_p(\psi > 0) - E_p(\psi < 0)$ (from [16]).

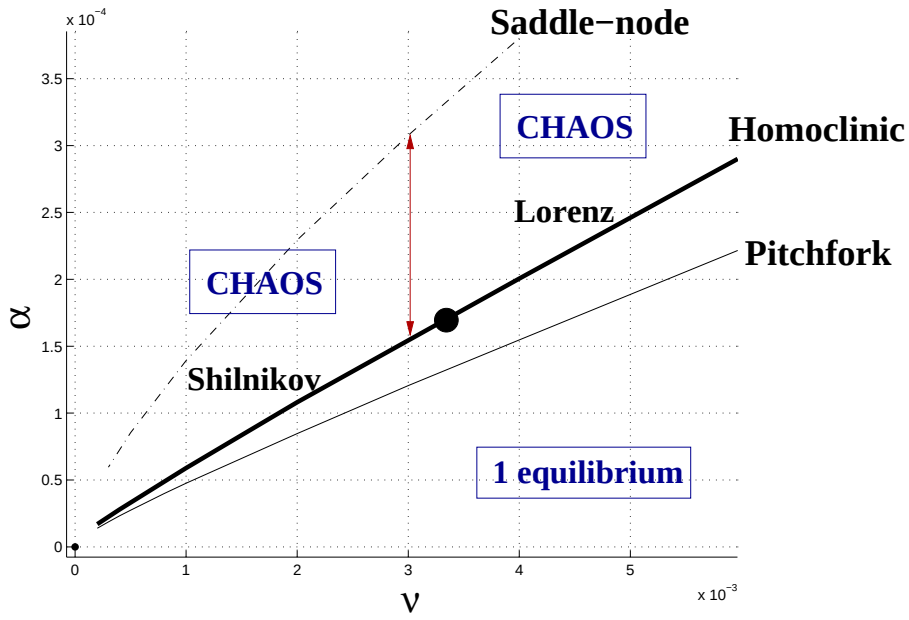

Figure 19: Loci of pitchfork (light solid curve), homoclinic (heavy solid curve) and saddle-node bifurcations (dash-dotted curve) in the 2-parameter plane spanned by the nondimensional viscosity ν and wind-stress intensity α. The filled circle marks the transition between Lorenz chaos and Shilnikov chaos. (from [16]).

For small ν, it appears that the homoclinic orbit is of saddle-focus type similar to the Shilnikov case [34] presented in section 2 although there is now an additional symmetry.

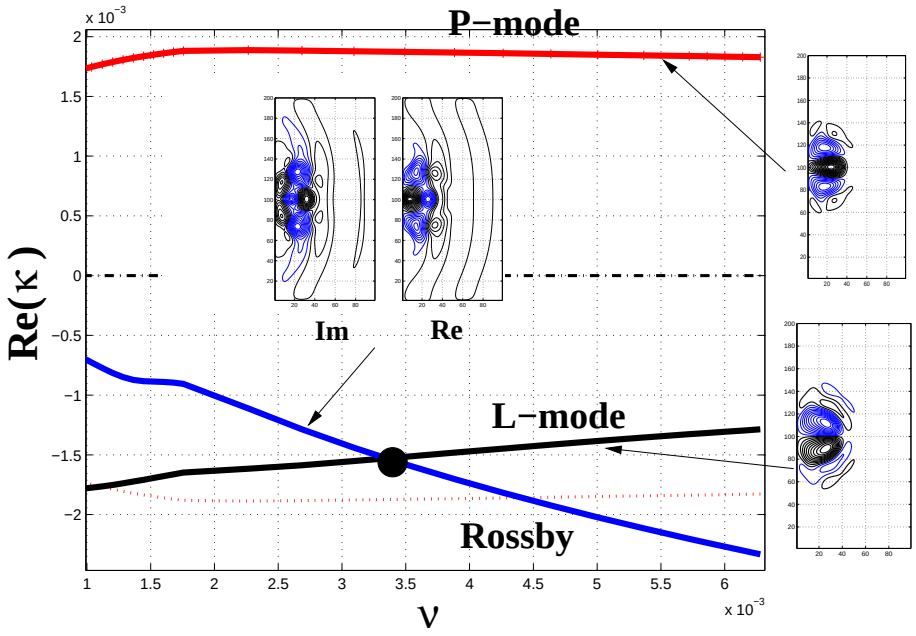

Figure 20: Leading instabilities that occur along the homoclinic locus of Fig. 19, as a function of the viscosity ν. The curves plotted in the large panel are the real parts of the leading eigenvalues (the ones closest to the imaginary axis). The spatial patterns of the associated streamfunction fields (real for the P- and L-mode and complex conjugate for the Rossby basin mode) are plotted in the small panels (from [16]).

Complex dynamics is found on both sides of the homoclinic orbit: A sketch of the bifurcations of periodic orbits in the vicinity of the principal homoclinic orbit is shown for values of the wind stress (ν fixed) near the critical value $\bar{\alpha}$ in Fig. 21. One thus observes period-doubling bifurcations of the periodic orbits related to the gyre modes for $\alpha < \bar{\alpha}$ similar to the ones observed in [6, 55] as well as symmetry-breaking bifurcations of the now symmetric limit cycles 'after' the homoclinic bifurcation. Note that each symmetry-breaking bifurcation provides a new family of asymmetric periodic orbits which undergo sequences of period-doubling bifurcations. This wiggling behavior is indeed confirmed directly by integrating the model (43) for many values of α near $\bar{\alpha}$ in [17] (not shown).

It is clear from bifurcation theory that one is limited to secondary bifurcations and that as further instabilities emerge, the dimensions of the chaotic attractors as well as their topological complexities increase. One may thus legitimately ask about the nature of chaos in the double-gyre circulation when the nonlinearity is increased

even further. A surprising answer is given in [67] which justifies even more the use of those dynamical systems concepts when the flows approach more turbulent states. As far as large oceanic basins like the North Atlantic and Pacific are concerned a new phenomenon emerges which has been referred to as *the quantization of the low-frequency dynamics* in [67]. Roughly speaking the successive bifurcations culminating with the symmetric homoclinic bifurcation as described previously are repeated but now involve larger wavenumbers. Figure 22 is indeed a generalization of Fig. 19. The first colored band corresponds exactly to the situation shown in Fig. 19 except that the saddle-node curve is now replaced by a locus of subcritical pitchfork birfurcations. Between the two curves, Shilnikov phenomena are observed (not shown). The next colored bands exhibit the same successive bifurcations namely supercritical pitchfork bifurcations, real eigenmode merging off the asymmetric branches of solutions like in Fig. 31 followed by Hopf bifurcations of gyre modes and finally subcritical pitchfork bifurcation. The unfolding of the relaxation oscillations (see Fig. 18) into a symmetric homoclinic orbit is not explicitly detected however. The reason is related to the appearance of high-frequency instabilities (through Hopf bifurcations) along the antisymmetric branch. These instabilities interact nonlinearly with the low-frequency structures (the gyre modes) so that the poor man's continuation approach is inefficient here.

There are at least two ways to detect the presence of a global bifurcation in this situation: the first is through statistical methods and spectral analysis like multichannel singular spectrum analysis (M-SSA) that we do not present here (see e.g. [69, 70]). The second is through continuation methods of periodic orbits which, as far as we know, have been used only in the work of [71, 72, 73] in a different context and for rather small to medium dimensional dynamical systems. The conclusion from [67] is that the low-frequency skeleton of the attractors in more nonlinear regimes is likely to be self-similar to the so-called 'ground regime' described at length above and that such a property can rather be easily detected using mere continuation techniques.

4.2 The shallow-water model

We discuss here an original example (unpublished) which uses the great strength and flexibility of continuation and homotopy methods. This example is directly connected to the problem of having explicit numerical control on the hierarchy of models available in geophysics. As seen previously the QG equations (43) satisfy the exact symmetry (44). One of the consequence is that the branches of steady states are all connected. In more complex models, such a property disappears and one is confronted to situations where it is, most of the time, difficult to detect the isolated branches. A typical situation is the case of the shallow-water (SW) equations that are given by

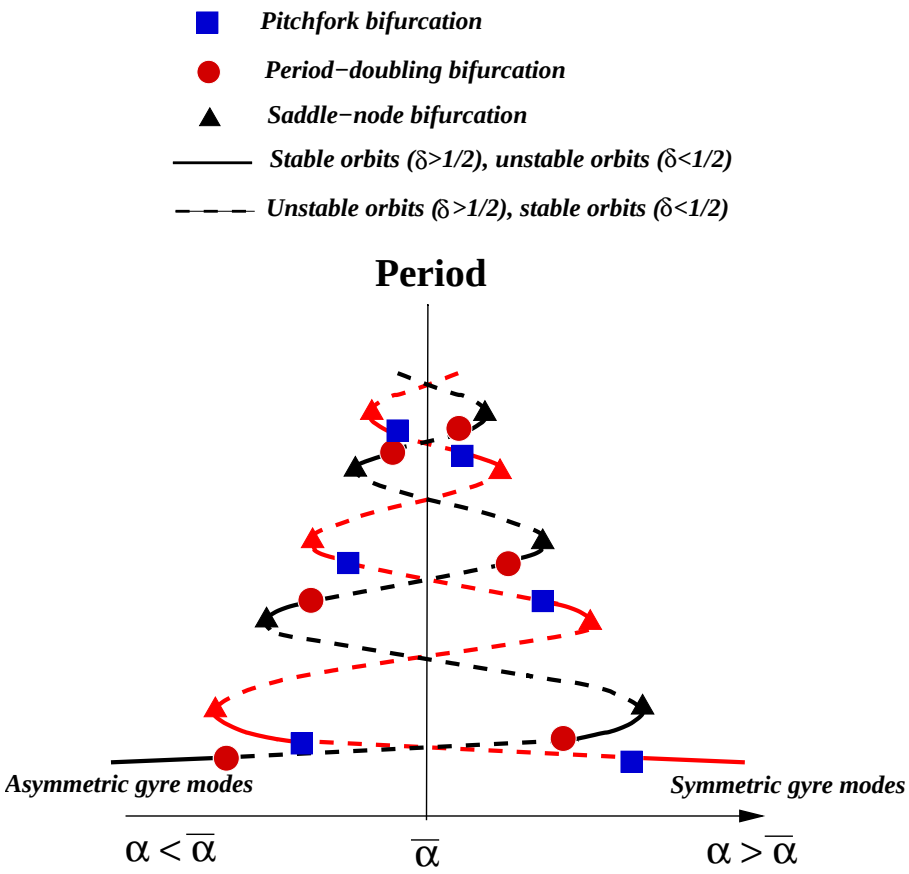

Figure 21: Shilnikov wiggles in the $\mathbb{Z}_2$-symmetric case and for $\delta < 1$. The period of the asymmetric periodic orbits (left curve) has been multiplied by 2.

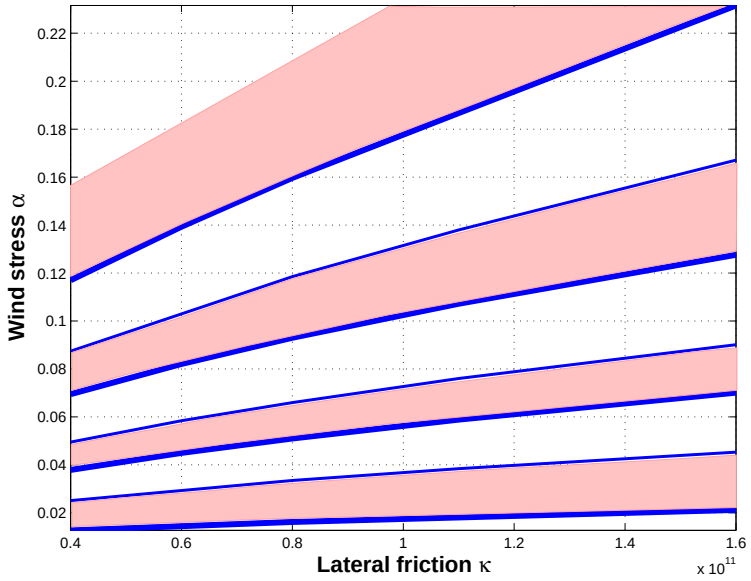

Figure 22: Loci of supercritical and subcritical pitchfork bifurcations The two-parameter plane is spanned by the wind-stress intensity α and the lateral hyper-viscosity κ. The shaded areas correspond to the n-bump supercritical regimes and the areas in-between to the n-bump subcritical regimes ($n = 0, 1, 2, 3$) (From [67]).

the following system

$$\begin{aligned} U_t + \nabla \cdot (\mathbf{v}U) - fV = & \quad -g'hh_x + \nu\Delta U - \mu U + \alpha\frac{\tau^x}{\rho} \\ V_t + \nabla \cdot (\mathbf{v}V) + fU = & \quad -g'hh_y + \nu\Delta V - \mu V + \alpha\frac{\tau^x}{\rho} \\ h_t = & \quad -U_x - V_y, \end{aligned} \tag{45}$$

where the eastward and northward velocities are given by $\mathbf{v} = (u, v)$ and h is the thickness of the upper layer. The upper-layer mass flux vector is represented by $\mathbf{V} = (U, V) = (uh, vh)$. The reduced gravity g' is given by $g' = g\Delta\rho/\rho$. The dissipative terms are given by the lateral friction coefficient ν and the bottom friction coefficient μ. We consider these equations, often referred to as *1.5-layer* or *equivalent-barotropic or reduced-gravity model*, in a closed domain Ω as in (43) together with either no-slip or free-slip boundary conditions. The double-gyre forcing term is given by

$$\tau^x = -\cos(\frac{2\pi y}{L_y}), \tau^y = 0.$$

It is straightforward to check that the system of equations (45) is no longer invariant with respect to the symmetry (44). Now, a close inspection shows that it is possible

to connect the system (43) to (45) through a so-called homotopy parameter η, namely

$$\begin{aligned}
&U_t + \eta\left[\nabla\cdot(\mathbf{v}U) + g'hh_x\right] + (1-\eta)\left[\nabla\cdot(\mathbf{V}U) + g'h_x\right] - fV = \nu\Delta U - \mu U + \alpha\frac{\tau^x}{\rho}\\
&V_t + \eta\left[\nabla\cdot(\mathbf{v}V) + g'hh_y\right] + (1-\eta)\left[\nabla\cdot(\mathbf{V}U) + g'h_y\right] + fU = \nu\Delta V - \mu V + \alpha\frac{\tau^y}{\rho}\\
&h_t + U_x + V_y = 0.
\end{aligned} \tag{46}$$

When $\eta = 0$, one recovers the steady-state version of Eq. (43) by taking the curl of (46) with $U = -\psi_y, V = \psi_x$ whereas $\eta = 1$ yields Eq. (45). It thus becomes possible to compute the branches of solutions for $\eta = 0$ and then smoothly going to the case $\eta = 1$ by pseudo-arclength continuation. The result is given in Fig. 23 for a small oceanic domain. Previous studies of SW models of the double-gyre circulation [52, 54, 55] were able to compute branches a and b in Fig. 23 but not branch c. The methodology is even more interesting in large basins since one observes successive pitchfork bifurcations in QG models which have never been computed in SW models.

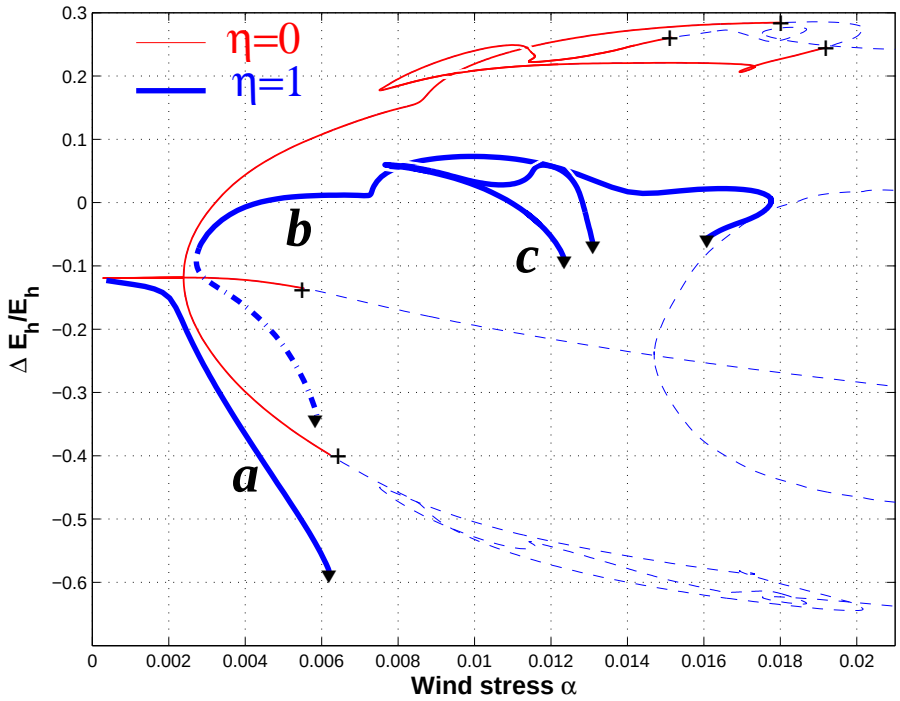

Figure 23: Branches of steady states for the system (46) for $\eta = 0$ (light curves) and $\eta = 1$ (thick curves). The thin dotted curves correspond to the case $\eta = 0$ which disappear when going to $\eta = 1$.

4.3 Bifurcations in primitive-equation models

Very recently, the double-gyre problem was considered in a 3-D primitive-equation model [61]. Similar as in the studies with quasi-geostrophic and shallow-water models, a basin of 10° length and 10° width centered around 45°N was considered. In longitude ϕ and latitude θ, the boundaries of the domain are given by $\phi_w = 270°\text{E}$, $\phi_e = 280°\text{E}$, $\theta_s = 40°N$ and $\theta_n = 50°N$; the basin has a constant depth D = 2400 m. The flows in this domain are forced by a zonal wind stress given by

$$\tau^\phi(\phi,\theta) = -\tau_0 \ \cos\left(2\pi\frac{\theta-\theta_s}{\theta_n-\theta_s}\right) \tag{47a}$$

$$\tau^\theta(\phi,\theta) = 0 \tag{47b}$$

where $\tau_0 = 0.1$ Pa is a typical amplitude. This wind forcing is distributed as a body forcing over the first (upper) layer of the ocean having a depth $H_m = 200$ m.

With $r_0 = 6.4 \cdot 10^6$ m and $\Omega = 7.5 \cdot 10^{-5}$ s^{-1} being the radius and angular velocity of the Earth, the governing equations for the zonal, meridional and vertical velocity u, v and w and the pressure p become

$$\frac{Du}{dt} - uv\tan\theta - 2\Omega\ v\sin\theta + \frac{1}{\rho_0\, r_0\cos\theta}\frac{\partial p}{\partial\phi} = A_V\frac{\partial^2 u}{\partial z^2} + A_H\, L_u(u,v) + \frac{\tau_0}{\rho_0 H_m}\tau^\phi\mathcal{G}(z) \tag{48a}$$

$$\frac{Dv}{dt} + u^2\tan\theta + 2\Omega\ u\sin\theta + \frac{1}{\rho_0\, r_0}\frac{\partial p}{\partial\theta} = A_V\frac{\partial^2 v}{\partial z^2} + A_H\, L_v(u,v) + \frac{\tau_0}{\rho_0 H_m}\tau^\theta\mathcal{G}(z) \tag{48b}$$

$$\frac{\partial p}{\partial z} = \rho_0 g \tag{48c}$$

$$\frac{\partial w}{\partial z} + \frac{1}{r_0\cos\theta}\left(\frac{\partial u}{\partial\phi} + \frac{\partial(v\cos\theta)}{\partial\theta}\right) = 0 \tag{48d}$$

where $\mathcal{G}(z) = \mathcal{H}(z/H_m + 1)$, $\mathcal{H}$ is a continuous approximation of the Heaviside function, $\rho_0 = 10^3$ kgm^{-3} is the constant density of the ocean water and $g = 9.8$ ms^{-2} is the gravitational acceleration. In these equations, A_H and A_V are the horizontal and vertical momentum (eddy) viscosity, respectively. We fix $A_V = 10^{-3}$ m^{2}s^{-1} and use

A_H as a control parameter. In addition,

$$\begin{aligned}
\frac{D}{dt} &= \frac{\partial}{\partial t} + \frac{u}{r_0 \cos\theta}\frac{\partial}{\partial \phi} + \frac{v}{r_0}\frac{\partial}{\partial \theta} + w\frac{\partial}{\partial z} \\
L_u(u,v) &= \nabla_H^2 u + \frac{u}{r_0^2 \cos^2\theta} - \frac{2\sin\theta}{r_0^2 \cos^2\theta}\frac{\partial v}{\partial \phi} \\
L_v(u,v) &= \nabla_H^2 v + \frac{v}{r_0^2 \cos^2\theta} + \frac{2\sin\theta}{r_0^2 \cos^2\theta}\frac{\partial u}{\partial \phi}
\end{aligned}$$

where ∇_H^2 is the horizontal Laplace operator. Slip conditions are assumed at the bottom boundary, while at all lateral boundaries no-slip conditions are applied. As the forcing is represented as a body force over the first layer, slip conditions also apply at the ocean surface.

The equations are discretized in space using a second-order accurate control volume discretization method on a staggered Arakawa B-grid with $i = 0, ..., N$, $j = 0, ..., M$, $k = 0, ..., L$. The solution vector $\mathbf{u}$ contains the unknowns (u, v, w, p) at each grid point and hence has dimension $d = 4 \times N \times M \times L$. A typical bifurcation diagram, with the lateral friction coefficient A_H as a control parameter, for a resolution of $100 \times 100 \times 12$ points is plotted in Fig. 24. In agreement to what is found in shallow-water models, we here also find an imperfect pitchfork bifurcation, which leads to the existence of multiple flow patterns below a value of $A_H = 320$ m^{2}s^{-1}. The isolated branch in Fig. 24 was found by the residue continuation algorithm as described in [8] and analyzed in [74].

The barotropic streamfunction of patterns at specific locations in Fig. 24 are plotted in Fig. 25. The solution for large A_H on the connected branch is the near anti-symmetric double-gyre flow (Fig. 25a). When A_H decreases along this branch, a so-called jet-down solution appears (Fig. 25b), a solution very well known from QG and SW models. Along the isolated branch, a jet-up solution exists (Fig. 25c) along the lower branch and after the saddle-node bifurcation, the flow becomes inertially controlled (Fig. 25d). Although these results were expected, this is the first time that such a multiple equilibria structure is computed for a 3-D primitive-equation model (a dynamical system having 480,000 degrees of freedom).

5 Outlook

Dynamical systems theory is a qualitative mathematical theory that deals with the spatio-temporal behavior of general systems of evolution equations. The theory analyzes systematically the changes in system behavior when parameters are varied. The brief overview in section 2 described the most elementary types of transitions,

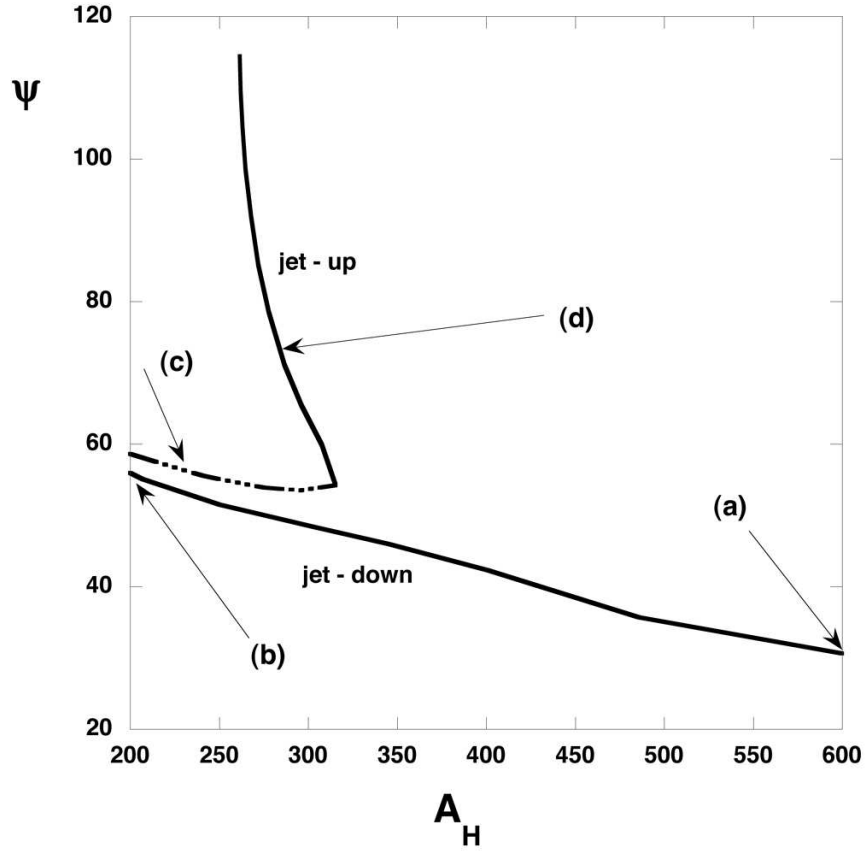

Figure 24: Bifurcation diagram of the constant density circulation and control parameter A_H.

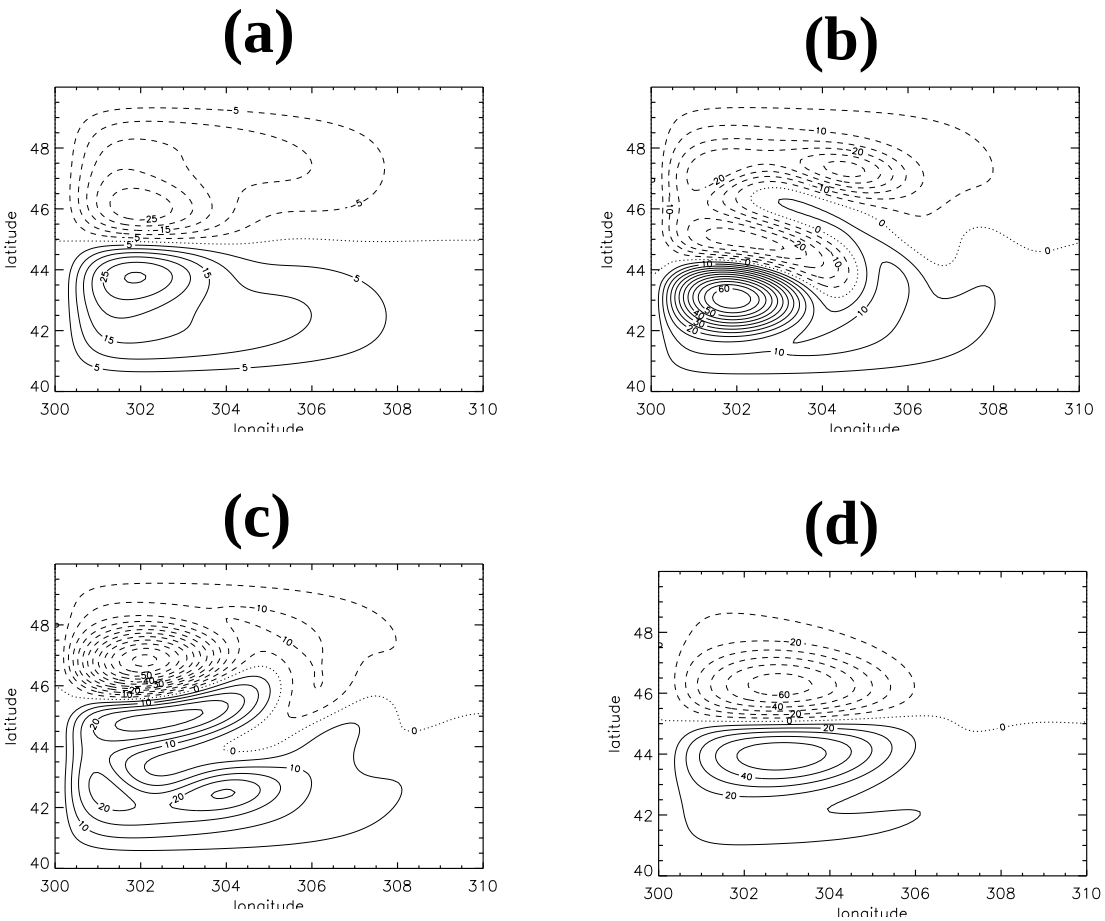

,

Figure 25: Patterns of the barotropic streamfunction (the streamfunction of the vertically integrated flow) at labelled solutions marked in Fig. 24. Contour values are in Sv (1 Sv = 10^6 m^3s^{-1}).

those associated with codimension-1 bifurcations. In [25, 28], the theory is further developed to deal with more complex transition scenarios.

The methodology of bifurcation theory was first applied in the 1960s and 1970s to highly simplified models of the ocean, atmosphere and climate, governed by systems of a few coupled ODEs [5, 31, 45, 46] or by one-dimensional PDEs [47, 48, 50]. The methodology of continuation methods and numerical bifurcation theory, briefly described in section 3, is now certainly capable of handling rather sophisticated models governed by 2-D and 3-D systems of PDEs. The systematic use of pseudo-arclength continuation algorithms coupled with linear stability analysis allows one to infer generic and meaningful information on the dynamics of large-scale flows. Local continuation techniques together with well-chosen time integrations enable one to detect global bifurcations as well. The use of a hierarchy of models is necessary to eliminate model-dependent dynamical processes and to focus on the essential dynamics.

The solutions of certain members of this hierarchy, such as the quasi-geostrophic (QG) equations (43), seem to be dominated by low-dimensional dynamics, embedded into an a priori infinite-dimensional phase space. This feature may be due to a significant separation of scales of motion; in the QG models, for example, the fast gravity waves are filtered out and only the dynamics related to low-frequency Rossby waves is represented. As far as the large scales are concerned, we might be able to view small-scale, fully developed turbulence as a background 'soup' that can be filtered out in the first approximation.

As an example of this approach, we considered a hierarchy of models of the constant-density, wind-driven double-gyre ocean circulation. It is possible to analyze the QG, shallow-water (SW) and primitive-equation (PE) models of this circulation systematically and to determine robust elements of the dynamics and of the transition behavior of these flows. We showed how to handle the corresponding PDEs as dynamical systems with a phase space of very large dimension and to detect and compute the successive bifurcations and branches of steady states. For example, the perfect pitchfork bifurcation associated with symmetry-breaking in the QG model is transformed into a perturbed pitchfork in the SW model and this imperfect pitchfork is still present in the PE model. Within the QG model, low-frequency variability originates from an oscillatory mode, the gyre mode. This mode, in turn, arises through the merging of two purely exponential modes and it subsequently causes global bifurcations associated with homoclinic orbits. The longest time scales involved in this low-frequency variability are of a few decades at most.

The effect of the small scales on the large ones is a difficult issue closely related to the system's spectral behavior. New, efficient coarse-graining bifurcation techniques have been recently developed by Y. Kevrekidis and colleagues (e.g. [75, 76]) in the context of chemistry and reaction-diffusion systems. These techniques enable models at a "fine," microscopic level of description, like the 3-D PE model presented in section 4.3, to perform modeling tasks at a "coarse," macroscopic level, like our QG models.

This feat is achieved by extracting from the microscopic description the information that traditional numerical procedures would obtain through function evaluation based on the macroscopic evolution equation, had this equation been available.

A characteristic feature of complex systems is the emergence of macroscopic, coherent types of behavior from the interactions of small-scale, microscopic elements. Macroscopic rules can therefore often be deduced from microscopic ones. Such is the case for the Navier-Stokes equations, which represent the (coarse) evolution of certain moments of the Boltzmann equation. In many situations, however, the macroscopic equations are not necessarily available. For instance, one may not have closed equations at the system level of interest, that is the macroscopic velocity field may not be available as a function of just concentrations, or the form of the viscous terms may not be just a known Newtonian expression. In these cases, one often has a correct microscopic description of the true physics, at a molecular level or at a very fine resolution, but system-level tasks are not feasible anymore, directly at the macroscopic level. Still, it turns out to be possible to use information from short-time integrations of the micro-models to obtain information on the macro-model's Jacobian and thus detect (macro-)bifurcations. It is only recently that these coarse-graining techniques are being tested in the context of geophysical fluid dynamics.

The methodology of dynamical systems is now being applied to many problems in physical oceanography and climate dynamics. Examples are (i) the stability and variability of the thermohaline circulation [77]; (ii) transitions in the El-Niño ocean-atmosphere system [8, 78, 79, 80], including those due to plate motion [81]; and (iii) variability of the mid-latitude atmosphere-ocean system [82]. This methodology is likely to provide a major avenue to understanding the processes that cause large-scale, low-frequency variability in the ocean, atmosphere and in the whole climate system.

Acknowledgements. MG's and ES's work was supported by Grants ATM00-82131 from the National Science Foundation's Programs on Climate Dynamics, Physical Oceanography, and Applied and Computational Mathematics, and DE-FG02-04ER63881 from the Department of Energy's Climate Change Prediction Program.

References

[1] S.H.Schneider and R.E.Dickinson. Climate modeling. *Rev. Geophys. Space Phys.*, 12:447–493, 1974.

[2] M.Ghil and A.W.Robertson. Solving problems with GCMs: General circulation models and their role in the climate modeling hierarchy. *General Circulation Model Developments: Past, Present and Future*, pages 285–325, 2000.

[3] H.A.Dijkstra and M.Ghil. Low-frequency variability of the large-scale ocean circulation: A dynamical systems approach. *Rev. Geophys.*, 43:RG3002, doi:10.1029/2002RG000122, 2005.

[4] I.M.Held. The gap between simulation and understanding in climate modeling. *Bull. Amer. Met. Soc.*, 86:1609–1614, 2005.

[5] H.Stommel. Thermohaline convection with two stable regimes of flow. *Tellus*, 2:230–244, 1961.

[6] S.Jiang F.F.Jin and M.Ghil. Multiple equilibria, periodic, and aperiodic solutions in a wind-driven, double-gyre, shallow-water model. *J. Phys. Oceanogr.*, 25:764–786, 1995.

[7] J.McCalpin and D.Haidvogel. Phenomenology of the low-frequency variability in a reduced-gravity, quasi-geostrophic double-gyre model. *J. Phys. Oceanogr.*, 26:739–752, 1996.

[8] H.A.Dijkstra. *Nonlinear Physical Oceanography, A Dynamical Systems Approach to the Large Scale Ocean Circulation and El Niño.* 2nd Revised and Enlarged Edition, Kluwer, Dordrecht/Boston/London, 532pp, 2005.

[9] P.Cessi and W.R.Young. Multiple equilibria in two-dimensional thermohaline circulation. *J. Fluid Mech.*, 241:291–309, 1992.

[10] C.Quon and M.Ghil. Multiple equilibria in thermosolutal convection due to salt-flux boundary conditions. *J. Fluid Mech.*, 245:449–484, 1992.

[11] C.Quon and M.Ghil. Multiple equilibria and stable oscillations in thermosolutal convection at small aspect ratio. *J. Fluid Mech.*, 291:33–56, 1995.

[12] O.Thual and J.C.McWilliams. The catastrophic structure of thermohaline convection in a two-dimensional fluid model and a comparison with low-order box models. *Geophys. Astrophys. Fluid Dyn.*, 64:67–95, 1992.

[13] Y.Feliks M.Ghil and E.Simonnet. Low-frequency variability in the mid-latitude atmosphere induced by an oceanic thermal front. *J. Atmos. Sci.*, 61:961–981, 2004.

[14] Y.Feliks M.Ghil and E.Simonnet. Low-frequency variability in the mid-latitude baroclinic atmosphere induced by an oceanic thermal front. *J. Atmos. Sci.*, sub judice, 2005.

[15] D.B.Chelton F.J.Wentz. Global microwave satellite observations of sea surface temperature for numerical weather prediction and climate research. *Bull. Amer. Met. Soc.*, 86:1097–1115, 2005.

[16] E.Simonnet M.Ghil and H.A.Dijkstra. Homoclinic bifurcations in the barotropic quasi-geostrophic double-gyre circulation. *J. Mar. Research.*, 63:931–956, 2005.

[17] E.Simonnet M.Ghil and H.A.Dijkstra. Quasi-homoclinic behavior of the barotropic quasi-geostrophic double-gyre circulation. *Chaos*, in preparation, 2007.

[18] R.Temam. *Infinite-dimensional dynamical systems in mechanics and physics*. Springer-Verlag., New-York, applied mathematical science, vol 68 edition, 643pp, 1997.

[19] M.Ghil and S.Childress. *Topics in Geophysical Fluid Dynamics: Atmospheric Dynamics, Dynamo Theory and Climate Dynamics*. Springer-Verlag., New-York/Heidelberg/Berlin, 485pp, 1987.

[20] S.P.Meacham. Low-frequency variability in the wind-driven circulation. *J. Phys. Oceanogr.*, 30:269–293, 2000.

[21] B.T.Nadiga and B.P.Luce. Global bifurcation of Shilnikov type in a double-gyre ocean model. *J. Phys. Oceanogr.*, 31:2669–2690, 2001.

[22] D.T.Crommelin. Homoclinic dynamics: a scenario for atmospheric ultralow-frequency variability. *J.Atmos.Sci.*, 59:1533–1549, 2002.

[23] P.Chossat and R.Lauterbach. *Methods in Equivariant Bifurcation and Dynamical Systems*. Advanced Series in Nonlinear Dynamics, vol. 15, World Scientific, Singapour, 2000.

[24] M.I.Golubitsky I.Stewart and D.G.Schaeffer. *Singularities and Group in Bifurcation Theory, Vol II*. Springer-Verlag, New-York, 533pp, 2000.

[25] J.Guckenheimer and P.Holmes. *Nonlinear Oscillations, Dynamical Systems and Bifurcations of Vector Fields*. Springer-Verlag., New-York/Berlin, scnd edition, 453pp, 1990.

[26] G.Iooss and D.D.Joseph. *Elementary Stability and Bifurcation Theory*. Springer-Verlag, 356pp, 1999. (2nd ed.).

[27] J.E.Marsden and M.McCracken. *The Hopf Bifurcation and its Applications*. Springer-Verlag, New-York, 1976.

[28] Y.A.Kuznetsov. *Elements of Applied Bifurcation Theory*. Springer-Verlag, 515pp, 1995.

[29] D.Ruelle and F.Takens. On the nature of turbulence. *Comm. Math. Phys.*, 20:167–192, 1971.

[30] S.Wiggins. *Global Bifurcations and Chaos: Analytical Methods*. Springer-Verlag (Applied Mathematical Sciences), 494pp, 1988.

[31] E.N.Lorenz. Deterministic non-periodic flow. *J. Atmos. Sci.*, 20:130–141, 1963.

[32] C.T.Sparrow. *Lorenz Equations: Bifurcations, Chaos, and Strange Attractors*. Springer-Verlag (Applied Mathematical Sciences), 269pp, 1983.

[33] W.Tucker. A rigorous ODE solver and Smale's 14th problem. *Found. Comput. Math.*, 2:53–117, 2002.

[34] L.P.Shilnikov. A case of the existence of a denumerable set of periodic motions. *Sov. Math. Dokl*, 6:163–166, 1965.

[35] P.Glendinning and C.Sparrow. Local and global behavior near homoclinic orbits. *J. Stat. Phys.*, 35:645–696, 1984.

[36] P.Glendinning. Bifurcations near homoclinic orbits with symmetry. *Phys. Lett.*, 103A:163–166, 1984.

[37] H.B.Keller. Numerical solution of bifurcation and nonlinear eigenvalue problems. *Applications of Bifurcation Theory, Academic Press*, pages 359–384, 1977.

[38] R.Seydel. *Practical Bifurcation and Stability Analysis: From Equilibrium to Chaos*. Springer-Verlag, New-York, 1994.

[39] W.J.Stewart and A.Jennings. A simultaneous iteration algorithm for real matrices. *ACM Trans. Math. Software*, 7:184–198, 1981.

[40] G.Golub and C.Van Loan. *Matrix Computations*. The Johns Hopkins University Press, London, 1996. third ed.

[41] G.L.G.Sleijpen and H.A.Van der Vorst. A Jacobi-Davidson iteration method for linear eigenvalue problems. *SIAM J. Matrix Anal. Appl.*, 17:410–425, 1996.

[42] K.E.Atkinson. *An introduction to Numerical Analysis*. Jon Wiley and Sons, 1976.

[43] J.Sanchez M.Net B.Garcia-Archilla and C.Simo. Newton-Krylov continuation of periodic orbits for Navier-Stokes flows. *J. Comp. Phys.*, 201:13–33, 2004.

[44] E.N.Lorenz. The mechanics of vacillation. *J. Atmos. Sci.*, 20:448–464, 1963.

[45] G.Veronis. An analysis of wind-driven ocean circulation with a limited number of Fourier components. *J.Atmos.Sci.*, 20:577–593, 1963.

[46] G.Veronis. Wind-driven ocean circulation. ii: Numerical solution of the nonlinear problem. *Deep Sea Research*, 13:31–55, 1966.

[47] I.M.Held and M.J.Suarez. Simple albedo feedback models of the ice caps. *Tellus*, 26:613–629, 1974.

[48] G.North. Analytical solution to a simple climate model with diffusive heat transport. *J.Atmos.Sci.*, 32:1301–1307, 1975.

[49] G.R.North J.G.Mengel and D.A.Short. Simple energy-balance model resolving the seasons and the continents - application to the astronomical theory of the ice ages. *J. Geophys. Res.*, 88:6576–6586, 1983.

[50] M.Ghil. Climate stability for a Sellers-type model. *J.Atmos.Sci.*, 33:6–20, 1976.

[51] B.Legras and M.Ghil. Persistent anomalies, blocking and variations in atmospheric predictability. *J. Atmos. Sci.*, 42:433–471, 1985.

[52] S.Speich H.A.Dijkstra and M.Ghil. Successive bifurcations in a shallow-water model applied to the wind-driven ocean circulation. *Nonlinear Processes in Geophysics*, 2:241–268, 1995.

[53] E.Simonnet R.Temam S.Wang M.Ghil and K.Ide. Successive bifurcations in a shallow-water ocean model. *Lecture Notes in Physics, Springer-Verlag*, 515:225–230, 1998.

[54] E.Simonnet M.Ghil K.Ide R.Temam and S.Wang. Low-frequency variability in shallow-water models of the wind-driven ocean circulation. Part I: steady-state solutions. *J. Phys. Oceanogr.*, 33:712–728, 2003.

[55] E.Simonnet M.Ghil K.Ide R.Temam and S.Wang. Low-frequency variability in shallow-water models of the wind-driven ocean circulation. Part II: Time-dependent solutions. *J. Phys. Oceanogr.*, 33:729–752, 2003.

[56] F.W.Primeau. Multiple equilibria of a double-gyre ocean model with super-slip boundary conditions. *J. Phys. Oceanogr.*, 28:2130–2147, 1998.

[57] F.Chen and M.Ghil. Interdecadal variability in an hybrid coupled ocean-atmosphere model. *J.Phys.Oceanogr.*, 26:1561–1578, 1996.

[58] H.A.Dijkstra H.Oksuzoglu F.W.Wubs and E.F.F.Botta. A fully implicit model of the three-dimensional thermohaline ocean circulation. *J. Comp. Phys.*, 173:685–715, 2001.

[59] W.Weijer H.A.Dijkstra H.Oksuzoglu F.W.Wubs and A.C.de Niet. A fully-implicit model of the global ocean circulation. *J. Comp. Phys.*, 192:452–470, 2003.

[60] F.Wubs A.C.De Niet and H.A. Dijkstra. The performance of implicit ocean models on b- and c-grids. *J. Comp. Phys.*, 211:210–228, 2006.

[61] A.C.De Niet F.W.Wubs A.Terwisscha van Scheltinga and H.A.Dijkstra. A tailored solver for bifurcation studies of high-resolution ocean models. *J. Comp. Phys.*, 227:654–679, 2007.

[62] J.Dengg A.Beckmann and R.Gerdes. The Gulf Stream separation problem. *The Warmwatersphere of the North Atlantic Ocean, Kraus,W.A. editor*, pages 253–290, 1996.

[63] J.Pedlosky. *Geophysical Fluid Dynamics*. Springer-Verlag., New-York/Heidelberg/Berlin, scnd edition, 710pp, 1987.

[64] J.C.McWilliams. A note on a consistent quasigeostrophic model in a multiply connected domain. *Dyn. Atmos. Oceans*, 1:427–441, 1977.

[65] E.Simonnet and H.A.Dijkstra. Spontaneous generation of low-frequency modes of variability in the wind-driven ocean circulation. *J. Phys. Oceanogr.*, 32:1747–1762, 2002.

[66] K.I.Chang K.Ide M.Ghil and C.-C.A. Lai. Transition to aperiodic variability in a wind-driven double-gyre circulation model. *J. Phys. Oceanogr.*, 31:1260–1286, 2001.

[67] E.Simonnet. Quantization of the low-frequency variability of the double-gyre circulation. *J. Phys. Oceanogr.*, 35:2268–2290, 2005.

[68] F.Takens. Detecting strange attractors in turbulence. *Lecture notes in Mathematics*, 898:366–381, 1981. In D.A. Rand and L.-S. Young (Eds), Springer.

[69] G.Plaut and R.Vautard. Spells of low-frequency oscillations and weather regimes in the northern hemisphere. *J. Atmos. Sci.*, 51:210–236, 1994.

[70] M.Ghil R.M.Allen M.D.Dettinger K.Ide D.Kondrashov M.E.Mann A.Robertson A.Saunders Y.Tian F.Varadi and P.Yiou. Advanced spectral methods for climatic time series. *Rev. Geophys.*, 10.1029/2000GR000092, 2002.

[71] S.M.Zoldi and H.S.Greenside. Spatially localized unstable periodic orbits of a high-dimensional chaotic system. *J.Atmos.Sci.*, 57:2511–2514, 1998.

[72] R.M.Samelson. Periodic orbits and disturbance growth for baroclinic waves. *J.Atmos.Sci.*, 58:436–450, 2001.

[73] C.L.Wolfe and R.M.Samelson. Normal-mode analysis of a baroclinic wave-mean oscillation. *J.Atmos.Sci.*, 63:2795–2812, 2006.

[74] I.Gruais N.Rittemard and H.A.Dijkstra. A priori estimations of a global homotopy residue continuation method. *Nonlinear Functional Analysis and Optimization*, 26, 4-5:507–521, 2005.

[75] C.W.Gear I.G.Kevrekidis and C. Theodoropoulos. Coarse integration/bifurcation analysis via microscopic simulators: micro-Galerkin method. *Comp. Chem. Engng.*, 26:941–963, 2002.

[76] I.G.Kevrekidis C.W. Gear J.M.Hyman P.G.Kevrekidis O.Runborg and C.Theodoropoulos. Equation-free multiscale computation: enabling microscopic simulators to perform system-level tasks. Physics/0209043 at arXiv.org.

[77] L. A. Te Raa and H. A. Dijkstra. Instability of the thermohaline ocean circulation on interdecadal time scales. *J. Phys. Oceanogr.*, 32:138–160, 2002.

[78] J.D.Neelin M.Latif and F.-F.Jin. Dynamics of coupled ocean-atmosphere models: the tropical problem. *Annu. Rev. Fluid Mech.*, 26:617–659, 1994.

[79] J.D.Neelin D.S.Battisti A.C.Hirst F.-F.Jin Y.Wakata T.Yamagata and S.Zebiak. ENSO theory. *J. Geophys. Res.*, 103:14261–14290, 1998.

[80] P.C.F. Van der Vaart H.A. Dijkstra and F.-F.Jin. The Pacific cold tongue and the ENSO mode: Unified theory within the Zebiak-Cane model. *J.Atmos.Sci.*, 57:967–988, 2000.

[81] A.W. Omta and H.A.Dijkstra. A physical mechanism for the Atlantic-Pacific flow reversal in the early Miocene. *Global and Planetary Change*, 36:265–276, 2003.

[82] Van der E. Avoird H.A.Dijkstra J.J.Nauw and C.J.E.Schuurmans. Nonlinearly induced low-frequency variability in a midlatitude coupled ocean-atmosphere model of intermediate complexity. *Clim. Dyn.*, 19:303–320, 2002.